TRANSIT TIME DEVICES

Transit time devices, which include IMPATTs, TRAPATTs, BARITTs, and so on are solid-state sources of microwave power. Among these devices, IMPATTs are by far the most important in view of their frequency range and power output, and show great promise of increasing application in the twenty-first century. We first present a detailed discussion of IMPATT diodes, and then proceed to TRAPATTs, BARRITTs, etc., whose operation is restricted to lower microwave frequencies.

IMPATT DIODES

IMPATT diodes have emerged, at the end of the twentieth century, as very powerful solid-state sources of microwaves, millimeter waves, and submillimeter waves, covering a wide frequency spectrum. The reported frequency range of IMPATT oscillators extends from below X band (6 GHz) to the submillimeter wave region. The CW power output from a single device is quite high: reported results indicate 12 W at 6 GHz (1), 1 W at 94 GHz, and 2.2 mW at 412 GHz (2). The vast frequency range and high power output should make the IMPATT a highly suitable device to meet the ever increasing communication needs of the world. IMPATTs have been used in microwave and millimeter-wave digital and analog communication systems and in radars for civilian purposes, and in missiles for defense systems.

IMPATT is an acronym for *impact avalanche transit time,* which reflects the mechanism of its operation. In its simplest form an IMPATT is a *pn* junction diode reverse-biased to breakdown, in which an avalanche of electron–hole pairs is produced in the high-field region of the device depletion layer by impact ionization. The transit of the carriers through the depletion layer leads to generation of microwaves or millimeter waves when the device is tuned in a microwave or millimeter-wave cavity as shown in Fig. 1. Microwave oscillations from a simple p^+nn^+ silicon diode reverse-biased to breakdown were first reported in 1965 by Johnston, Deloach, and Cohen (3) from Bell Laboratories, but the same was earlier predicted by Read (4) for a special doping profile (p^+nin^+). It was later found that *pn* junctions of various doping profiles based on any semiconductor would give rise to IMPATT oscillations, and oscillations have been observed in Ge, Si, GaAs, and InP diodes.

The thin depletion layer of an IMPATT diode is subjected to high field at breakdown voltage, and the important high-field phenomena underlying IMPATT action are (1) saturation of drift velocity of charge carriers and (2) charge multiplication by impact ionization.

Saturation of Drift Velocity

In most semiconductors the drift velocity increases linearly with electric field according to Ohm's law in the low-field range, when the acoustic phonons are the main scattering agencies. At high field ($E > 10^6$ V/m) the dominant scattering mechanism is that by optical phonons arising from high-frequency thermal vibrations of the lattice, and the drift velocity of the charge carriers saturates as shown in Fig. 2 for Si, GaAs, and InP (5–8). An approximate expression for the

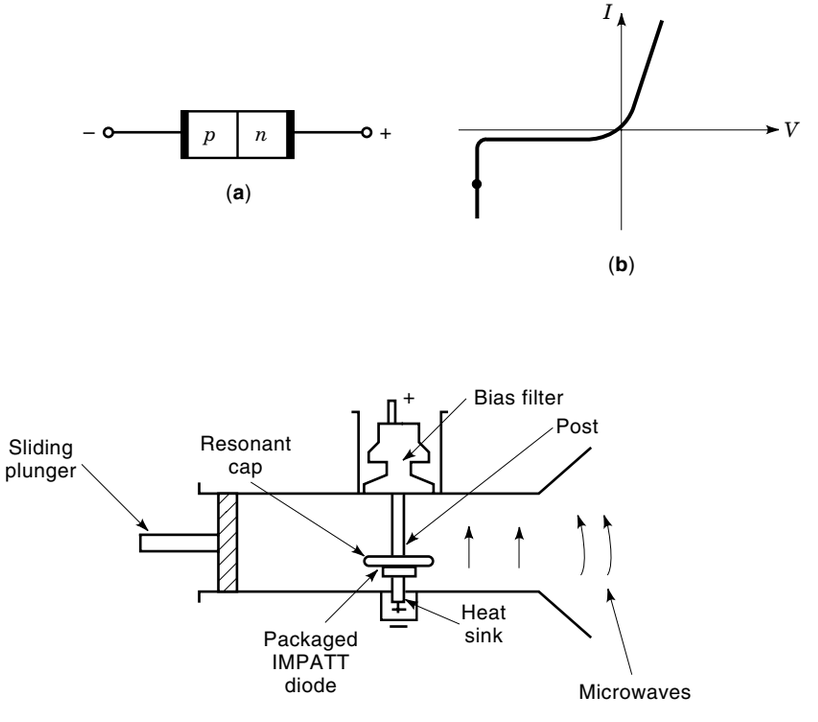

Figure 1. Schematic diagram of (a) basic IMPATT structure, (b) dc operating point, (c) microwave IMPATT oscillator.

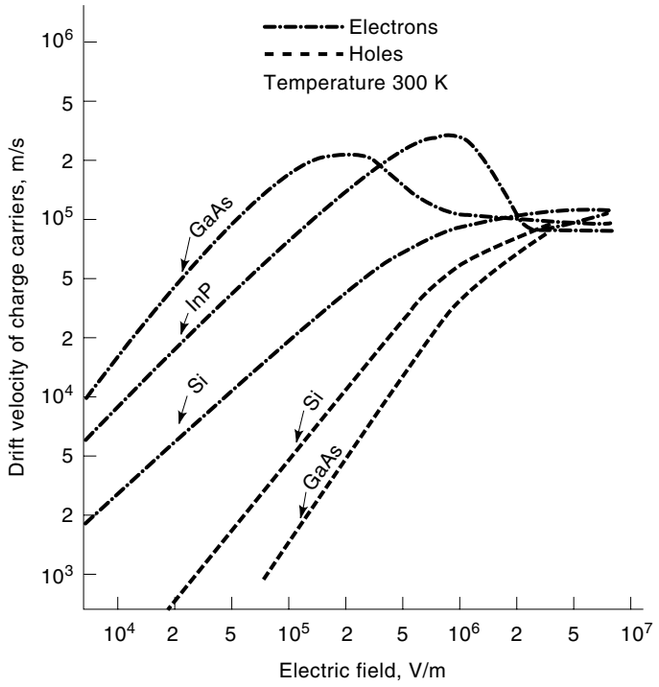

Figure 2. Drift velocity versus electric field for electrons in Si, GaAs, and InP and for holes in Si and GaAs (after Refs. 5–8).

saturated drift velocity of charge carriers, V_s, is

$$\left(\frac{8E_{\text{op}}}{3\pi m^*}\right)^{1/2}$$

where E_{op} is the optical phonon energy and m^* is the effective mass of the carriers. Thus the transit time required by charge carriers to cross the depletion region is proportional to the width of the depletion layer, since the velocity is constant at high field.

Impact Ionization, Carrier Multiplication, and Junction Breakdown

At higher fields (10^7 V/m and above), a carrier may gain enough energy from the electric field to reach the ionization threshold, when it can make an impact on an electron bound in the valence band and lift it to the conduction band, thereby creating a mobile electron in the conduction band and a mobile hole in the valence band. This process is known as the creation of an electron–hole (e–h) pair by impact ionization.

The ionization rates α_n and α_p for electrons and holes are defined to be the number of e–h pairs produced by an electron or hole per unit distance of travel in the direction of the electric field and are very strong functions of the electric field. The experimental results are approximately fitted with the empirical formula

$$\alpha_{n,p} = A_{n,p} \exp\left(\frac{B_{n.p.}}{E}\right) \tag{1}$$

where $A_{n,p}$ and $B_{n,p}$ are constants for a semiconductor.

Ionization rates for IMPATT-related semiconductors (Ge, Si, GaAs, and InP) have been measured by several workers (9–12) and are shown in Fig. 3. Repeated multiplication of charge carriers, like an avalanche, takes place by impact ionization in the high-field region around a junction biased to breakdown. When a small reverse saturation electron or hole current enters either edge of the depletion layer of a reverse-biased junction, the current is infinitely multiplied by the high field around the junction and the junction undergoes avalanche breakdown as shown in Fig. 4.

The current multiplication factor is related to the ionization rates of charge carriers in the depletion layer and is given by (12)

$$\int_0^W \overline{\alpha}\, dx = 1 - \frac{1}{M} \tag{2}$$

where

$$\begin{aligned} \overline{\alpha} &= \alpha_n \exp\left[-\int_0^x (\alpha_n - \alpha_p)\, dx'\right] \\ W &= \text{depletion layer width} \\ M &= \text{current multiplication factor} \end{aligned} \tag{3}$$

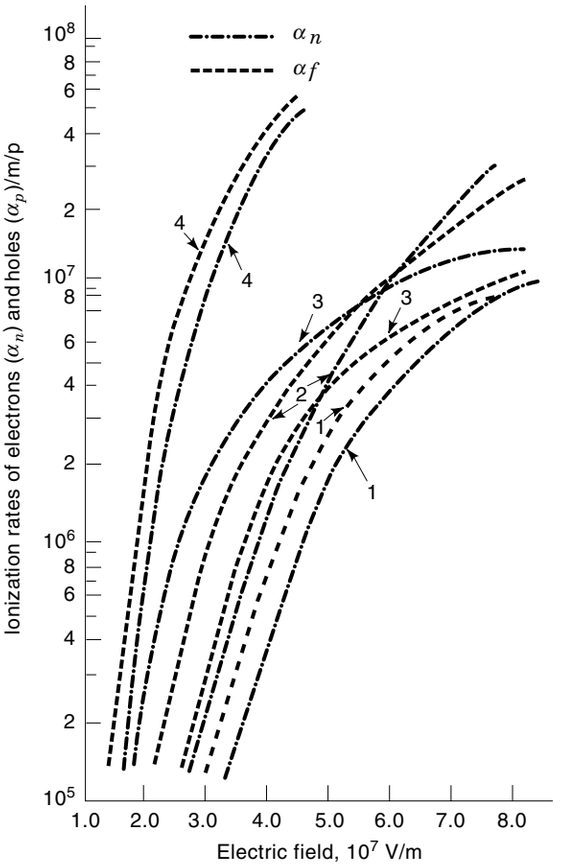

Figure 3. Ionization rate of electrons and holes in semiconductors versus electric field: 1, InP; 2, GaAs; 3, Si; 4, Ge (after Refs. 9–12).

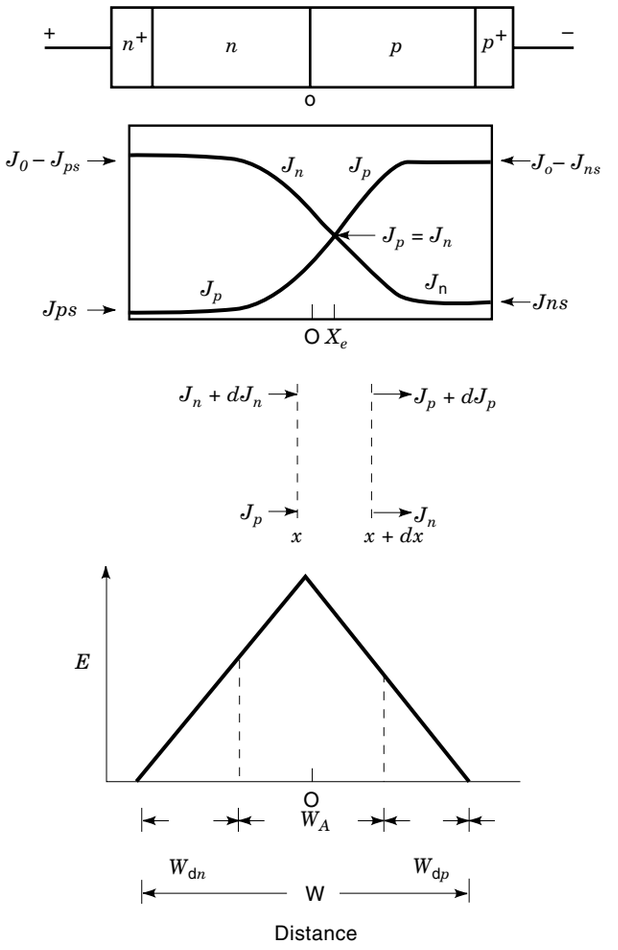

Figure 4. A *pn* junction under avalanche breakdown showing profiles of electron and hole current density and the electric field J_{ns}, J_{ps} = electron and hole saturation current densities; W_A = avalanche zone; W_{dn}, W_{dp} = electron and hole drift zones; X_C = avalanche center ($J_p = J_n$); W = depletion layer width.

The breakdown condition is reached when M tends to infinity and is given by

$$\int_0^W \overline{\alpha}\, dx = 1 \tag{4}$$

If $\alpha_n = \alpha_p = \alpha$, the breakdown condition is given by

$$\int_0^W \alpha\, dx = 1$$

The variation of avalanche breakdown voltage V_B, depletion layer width W, and maximum field at breakdown versus background doping concentration was studied and presented by Sze and Gibbons (13) for a one-sided abrupt junction in Ge, Si, and GaAs. The results indicate sharp fall of V_B and W with increasing background doping.

The depletion layer of an IMPATT diode is commonly divided into a high-field avalanche region of width W_a, where most of the multiplication takes place, and the lower-field drift region, where the field is high enough for carriers to move with saturated velocity but not high enough for charge multiplication along their path. It is usual to define the avalanche zone width

$$W_a \text{ by } \int_0^{W_a} \overline{\alpha}\, dx = 0.95$$

so that 95% of the impact ionization takes place in avalanche zone. Charge carriers emerge in large numbers from the avalanche zone and interact with the field while crossing the drift zone. This interaction leads to the generation of high-frequency oscillations.

IMPATT STRUCTURES AND DOPING PROFILES

The doping profile of IMPATT diodes can be varied to produce various field distributions and corresponding avalanche and drift zones. The three basic types of IMPATTs are (1) single drift region (SDR), (2) double drift region (DDR), and (3) double avalanche region (DAR) structures with flat doping profile in active regions. The SDR diode consists of a single avalanche zone and a single drift zone, and was first proposed by Read with p^+nin^+ structure. A simple SDR is usually realized as p^+nn^+. The doping density for p^+ and n^+ regions is around 10^{20} atoms/cm^3, for p and n regions is between 10^{16} and 10^{17} atoms/cm^3, and for an i region is around 10^{13} atoms/cm^3. A DDR diode has a p^+pnn^+ structure that consists of two drift layers, one for electrons and the other for holes, on either side of the central avalanche zone. Electrons and holes emerge from the central avalanche zone and move respectively towards the positive and negative terminals of the device with saturated drift velocity. The DDR diode produces more high-frequency power than the SDR, as a contribution to the power is made by each type of carriers in the corresponding drift zone. A DAR diode has a p^+nipn^+ structure that consists of one drift zone sandwiched between two avalanche zones (14). The electrons and holes from the two junctions at either end travel across the central i region in opposite directions and deliver power. Due to cancellation of mobile space charge in the central drift region, the DAR has very little distortion of field profile in the presence of a large mobile space charge.

Impurity charge bumps can be suitably introduced in the depletion layer by *molecular beam epitaxy* (MBE) or by ion implantation to produce high-efficiency low–high–low or high–low IMPATT diodes. The doping profiles are designed so that the resulting electric field profiles may constrict the avalanche zone. Thus one can have high–low or low–high–low IMPATT diodes with SDR or DDR structures where the avalanche zone can be suitably constricted by impurity bumps to realize high efficiency. The doping profiles of SDR and DDR structures with flat and low–high–low doping, as well as for DAR and *pin* diodes, are shown in Figs. 5 and 6 with the corresponding distributions of the electric field.

BASIC PRINCIPLE OF GENERATION OF MICROWAVES IN IMPATT DIODES

Microwave generation in an IMPATT diode can be explained using a simple SDR structure. In an SDR (Read or p^+nn^+ or

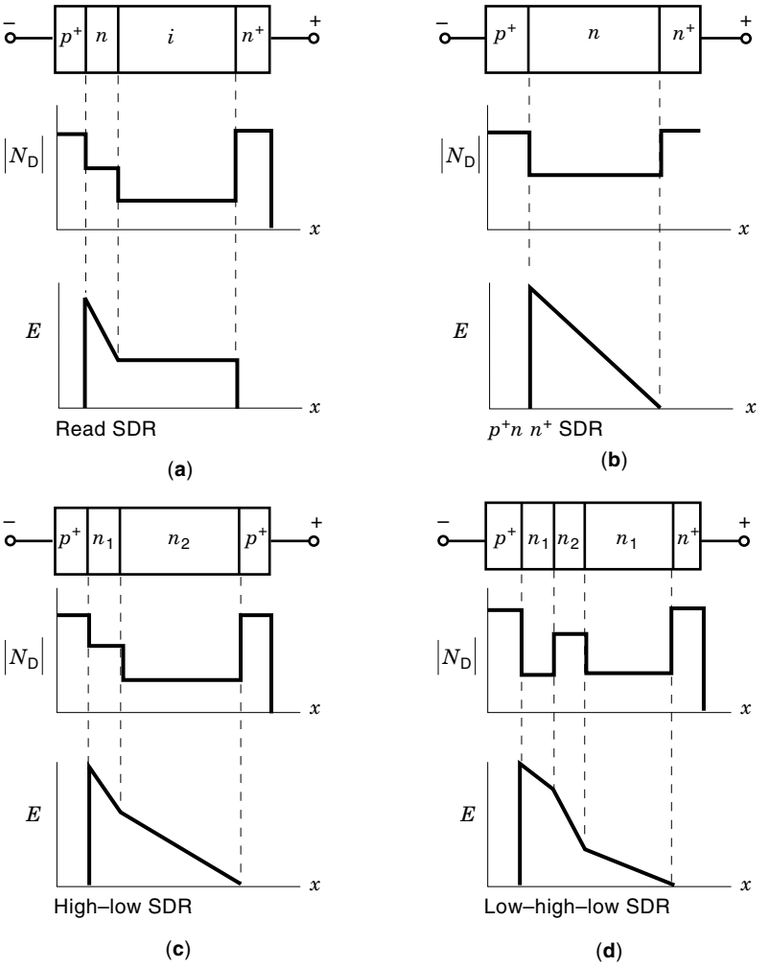

Figure 5. Structure, doping profile, and electric field profile of (a) Read SDR, (b) p^+nn^+ SDR, (c) high–low SDR, (d) low–high–low SDR.

n^+pp^+) the narrow avalanche zone situated at the junction end of the depletion layer is followed by a drift zone. If a sinusoidal electric field is applied to a device biased to the threshold of dc breakdown, an avalanche of e–h pairs is created in the avalanche zone. The number of e–h pairs created reaches its peak after the peak of the ac field has passed. This is because the number of e–h pairs created is proportional to the product of ionization rate of an individual carrier, which is highest at the instant of the peak field, and the number density of charge carriers present. Since the number density goes on increasing as long as the applied field is added to the dc field, the peak of e–h pair creation is delayed with respect to the peak of ac field by a phase angle approximately equal to 90°. This delay is called the avalanche buildup time. The charge pulse thus formed is delayed by $\pi/2$ with respect to peak of the ac field; it then crosses the drift zone with saturated velocity and produces a constant induced current in the external circuit during the time of transit, W/v_s.

Thus one gets a positive rectangular current pulse when the ac field superimposed on the dc field is negative (Fig. 7). The fundamental component of this current is therefore in antiphase with the ac field, which causes a negative high-frequency resistance. The avalanche buildup time delay together with transit time delay leads to approximately 180° phase delay between the ac current and the applied ac voltage, leading to a high-frequency negative resistance. That oscillations are generated by IMPATT diodes in the microwave frequency range can be understood by taking the example of a common silicon (p^+nn^+ SDR) device with n-region width w. The time required to cross w with drift velocity v_s is w/v_s. Thus half the time period of oscillations is given by w/v_s and the frequency by $f = v_s/2w$. For a typical n-layer thickness of 5 μm and drift velocity of 10^5 m/s, we have $f = 10^5/(2 \times 5 \times 10^{-6})$ Hz $= 10^{10}$ Hz = 10 GHz. Thus in principle 100 GHz can be generated by simply taking an approximately 10 times thinner epitaxial layer, i.e. 0.5 μm.

SMALL-SIGNAL ANALYSIS BASED ON ANALYTICAL APPROXIMATION

In order to understand the high-frequency properties of IMPATTs, Read undertook a small-signal analysis of the SDR, which was further improved by Gilden and Hines (15). For the sake of analytical convenience, the ionization rates and drift velocities were considered identical ($\alpha_n = \alpha_p$, $v_{ns} = v_{ps}$) and small sinusoidal variations of electron density, hole density, and electric field were imposed on dc quantities. The di-

ode impedance is approximately given by (15)

$$Z = \frac{w_D^2}{2Av_s\epsilon_s(1-\omega^2/\omega_a^2)} + R_s + \frac{j}{\omega C}\left(\frac{1}{\omega_a^2/\omega^2 - 1}\right) \qquad (5)$$

where ω is the angular frequency, w_D is the width of the drift zone, A is the diode area, R_s is the parasitic positive series resistance due to substrate and undepleted epitaxial region, ϵ_s is the dielectric constant, $C = \epsilon_s A/W$ is the total depletion region capacitance, W is the depletion region width, and ω_a is the avalanche resonance frequency given by $\omega_a = (2\alpha' v_s J_0/\epsilon_s)^{1/2}$, where $\alpha' = \delta\alpha/\delta E$ in the avalanche zone and J_0 is the dc current density.

This shows that the diode resistance becomes negative when $\omega > \omega_a$. The diode reactance is inductive for $\omega < \omega_a$ and capacitive for $\omega > \omega_a$. The value of R_s must be less than the magnitude of the active negative resistance for oscillation to take place. The schematic diagram and the equivalent circuit of the avalanche zone of the Read SDR diode, the equivalent circuit of the Read diode for small transit angle, and the variation with frequency of the real and imaginary parts of the active impedance are shown in Fig. 8 and 9. The avalanche zone behaves as a parallel LC resonant circuit with resonant frequency ω_a as shown in Fig. 8(b), where $L_a = W_a/2J_0\alpha' A\, v_d$ and $C_a = \epsilon_s A/W_a$.

COMPUTER STUDIES OF THE DC AND SMALL-SIGNAL PROPERTIES OF IMPATT DIODES OF ANY DOPING PROFILE

Computer studies are essential for understanding the properties of IMPATT diodes, as the analytical methods do not provide accurate information regarding the dc and high-frequency parameters of these devices. Further, analytical methods incorporate unrealistic assumptions regarding the ionization rates and their field variation and also regarding the extents of the avalanche and drift layers. Computer methods have been developed by several workers (16,17) that can

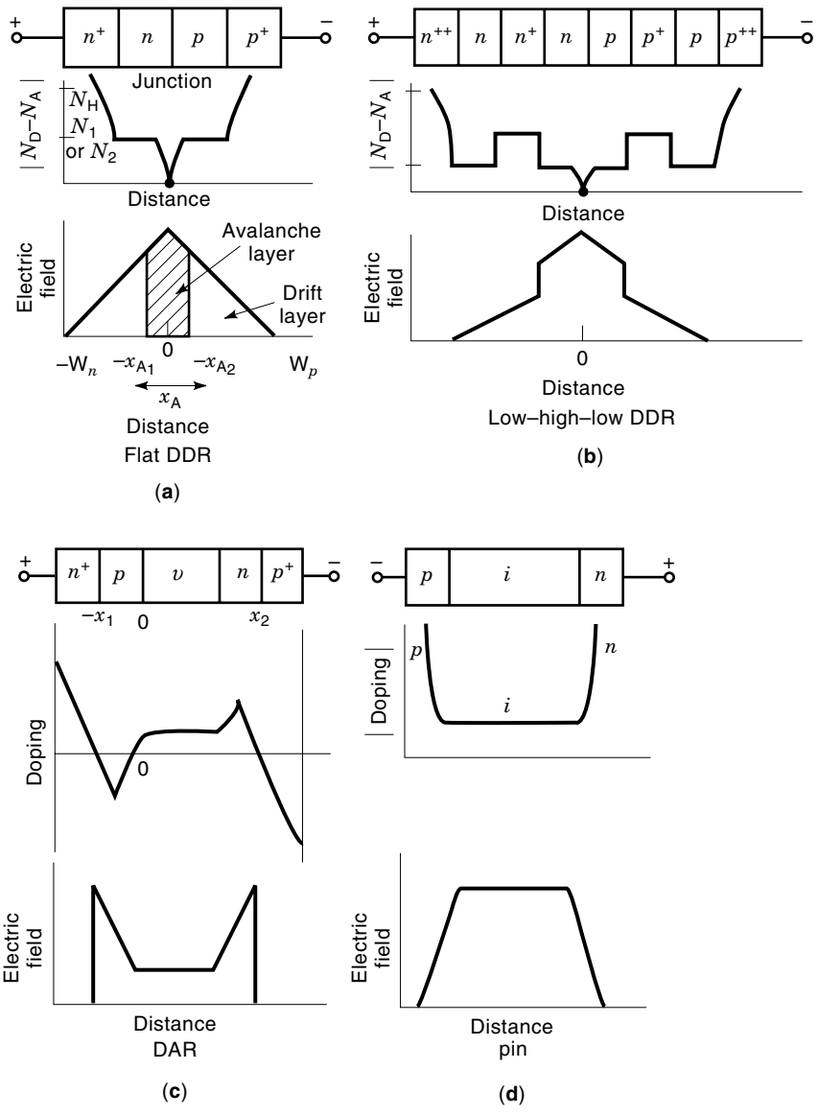

Figure 6. Structure, doping profile, and electric field profile of (a) flat DDR, (b) low–high–low DDR, (c) DAR, (d) *pin*.

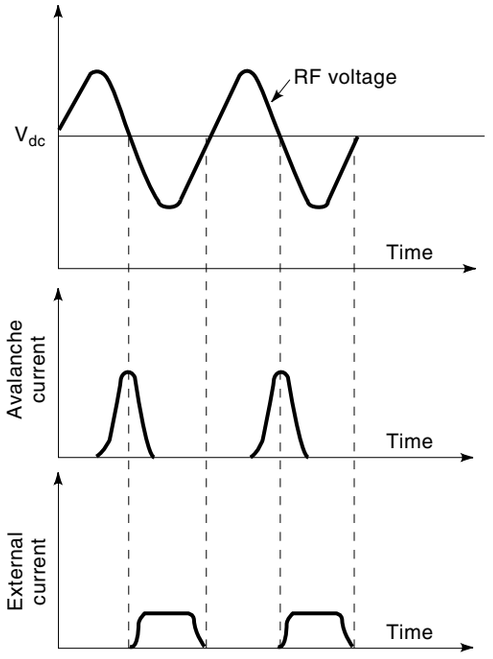

Figure 7. Waveforms of RF voltage, avalanche current, and induced external current in a Read diode (15).

provide accurate and realistic dc data on carrier current and field profiles in the depletion layer. The high-frequency properties of the device can be computed from the dc data.

In this section we will present a simple computer method for dc field and current profiles in IMPATT devices starting from the field maximum in the depletion layer. The field profile of IMPATT diodes generally exhibits a field maximum near the metallurgical junction. Dc field and current profiles for various IMPATT structures that involve simultaneous computer solution of nonlinear Poisson and continuity equations can be obtained by starting the computation from the field maximum within the depletion layer. The field maximum method is suitable for any arbitrary doping profile and involves the determination of the location and magnitude of the field maximum (18). In earlier methods, these equations were solved numerically, starting from one edge of the depletion layer. The location x_i of one edge is adjusted by iteration until the boundary conditions for the carrier current and the electric field are satisfied at the other edge. However, the matching of the boundary condition is difficult because the relative changes of the electric field are extremely sharp at the two edges of the depletion layer, and a slightly wrong choice of x_i may lead to numerical instability (17). The field maximum method, on the other hand, leads to quick solution for the boundary condition and is specially suitable for high dc current density when the mobile space charge effect is large.

With increasing dc current density there is not only a change in the magnitude of the field maximum (E_0) but also a shift in its position (x_0) away from the metallurgical junction. The shift depends on the inequality of ionization rates of the two types of carriers and increases with dc current density; though small, it is important for satisfying the boundary

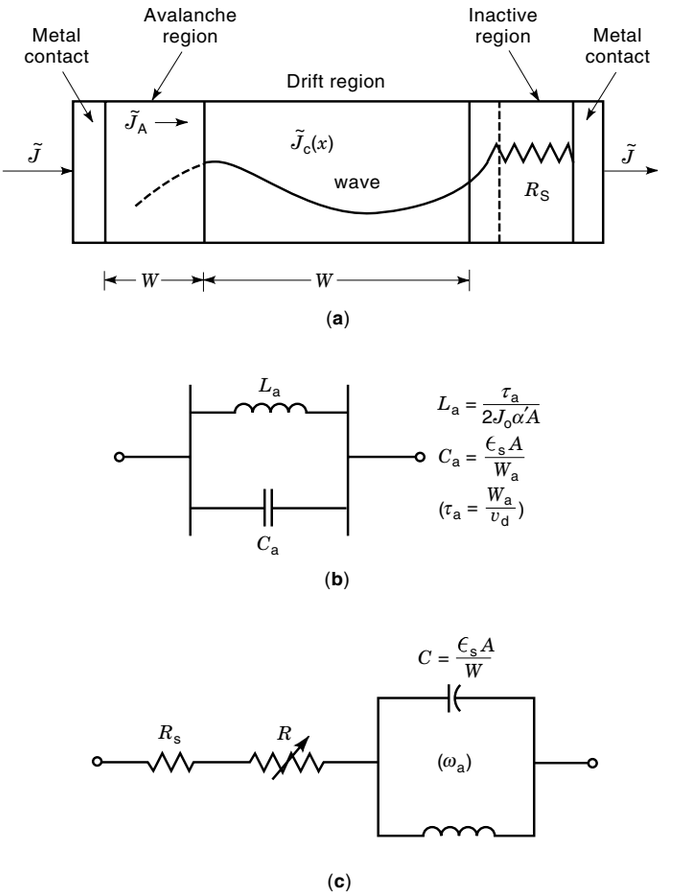

Figure 8. (a) Schematic diagram of avalanche, drift, and inactive regions of a Read diode. (b) Equivalent circuit of the avalanche zone of a Read diode. (c) Equivalent circuit of a Read diode for small transit angle. (Taken from Ref. 15 with permission from IEEE.)

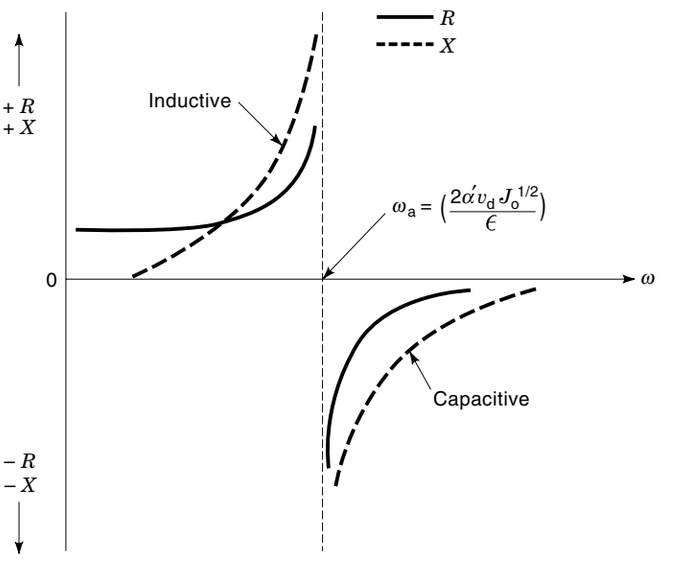

Figure 9. Resistance–reactance plot of a Read diode against frequency. (Taken from Ref. 15 with permission from IEEE.)

conditions. Hence a simultaneous solution of the Poisson and continuity equations is necessary to incorporate the effect of mobile space charge.

Basic Equations

The basic equations that govern the avalanche multiplication and the carrier current flow across the junction of an IMPATT diode are the Poisson equation

$$\frac{dE}{dx} = \frac{v}{\epsilon}(N_D - N_A + p - n) \tag{6}$$

and the carrier current continuity equations

$$\frac{dJ_p}{dx} = \alpha_n J_n + \alpha_p J_p \tag{7}$$

$$\frac{dJ_n}{dx} = -\alpha_n J_n - \alpha_p J_p \tag{8}$$

where the symbols have their usual significance. Combining Eqs. (7) and (8), one can obtain

$$\frac{dP(x)}{dx} = (\alpha_n + \alpha_p) - (\alpha_n - \alpha_p)P(x) \tag{9}$$

where $P(x) = [J_p(x) - J_n(x)]/J$. Determination of $P(x)$ fixes the values of $J_n(x)$ and $J_p(x) = 0.5J[1 \mp P(x)]$.

The numerical values of actual field dependence of the experimentally obtained values of ionization rates and drift velocities can be used in the method.

Computer Method

At the field maximum point $x = x_0$ near the metallurgical junction ($x = 0$), we have $(dE/dx)_{x=x_0} = 0$ and

$$P(x_0) = \frac{(v_p - v_n) - (2v/J)v_p v_n (N_D - N_A)|_{x=x_0}}{v_P + v_n} \tag{10}$$

The boundary conditions for the profiles $E(x)$ and $P(x)$ at the two edges of the depletion layer are given by $E(-x_1) = 0$, $P(-x_1) = -1$ and $E(x_2) = 0$, $P(x_2) = 1$. The numerical calculation for the simultaneous solution of the equations starts from the field maximum with assumed values of E_0 and x_0. The value of $P(x_0)$ is determined by E_0 and x_0 from Eq. (10). A double iteration over the values of E_0 and x_0 is carried out until the boundary conditions are satisfied at both ends of the depletion layer. Once E_0 and x_0 are fixed for a particular dc current density and doping profile, accurate $E(x)$ and $P(x)$ profiles are readily obtained. The method has been applied successfully to study the space charge effect at high current density for single-drift and double-drift IMPATT diodes (18). The values of E_0 and x_0 for different current densities are shown in Fig. 10 for a symmetrical DDR (n^+npp^+) structure (18). Corresponding field and current profiles of the same device for various current densities will be discussed later in connection with mobile space charge effects.

The field maximum method is highly suitable for studying the properties of DDR millimeter-wave diodes. Thus the electric field profiles of silicon DDRs for different window frequencies of 94, 140, and 220 GHz along with the absorption frequency of 60 GHz are shown in Fig. 11 for respective

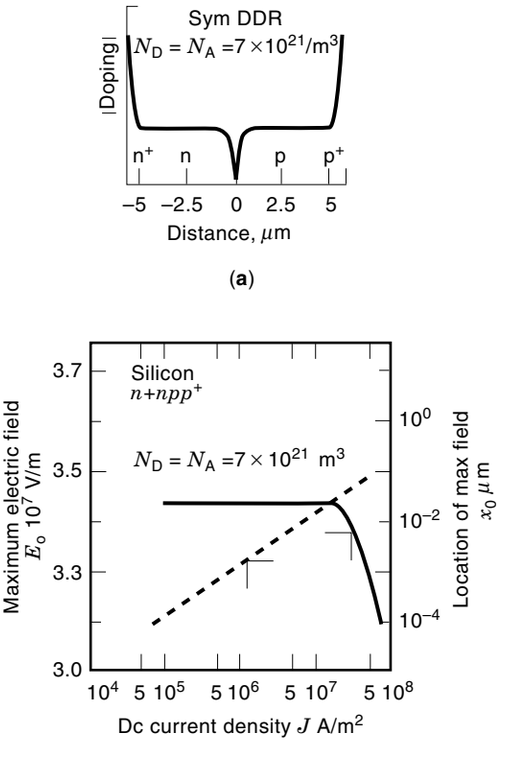

Figure 10. (a) Doping profile of n^+npp^+ structure and (b) plot of field maximum (E_0) and location (X_0) of maximum field against dc current density J for a DDR structure ($n = p = 7 \times 10^{21}$ m^{-3}).

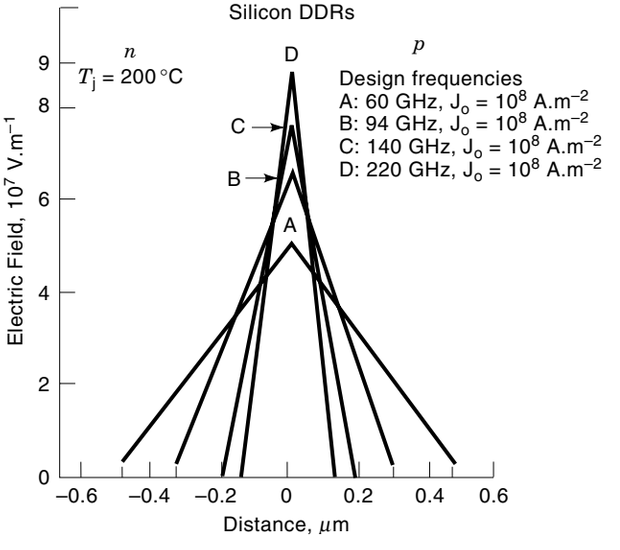

Figure 11. Electric field profiles of silicon DDRs for various design frequencies.

optimized current densities (19). It is seen that the magnitude of the field maximum increases sharply with increase of frequency while the width of the active layer becomes progressively thinner at higher frequencies.

SMALL-SIGNAL COMPUTER ANALYSIS OF IMPATT DIODES

Small-signal analysis of an IMPATT diode provides insight into the microwave performance of the device. If the ac field in the depletion region is very small compared to the dc breakdown field, the variation of ionization rate with electric field can be assumed to be linear and small-signal solution of time-varying Poisson and continuity equations can be carried out by linearization, which represents the low-amplitude limit of large-signal analysis. Gummel and Blue (20) presented a small-signal analysis of the basic equations free from simplifying assumptions regarding carrier properties. Following their approach, two second-order equations can be derived for the real (R) and imaginary (X) parts of the diode impedance $Z(x, \omega)$ for any point in the depletion layer:

$$\frac{d^2R}{dx^2} + (\alpha_n - \alpha_p)\frac{dR}{dx} - 2r\frac{\omega}{v}\frac{dX}{dx} + \left(\frac{\omega^2}{v^2} - H\right)R - 2\alpha\frac{\omega}{v}X - \frac{2\alpha}{v\epsilon} = 0 \tag{11}$$

and

$$\frac{d^2X}{dx^2} + (\alpha_n - \alpha_p)\frac{dX}{dx} + 2r\frac{\omega}{v}\frac{dR}{dx} + \left(\frac{\omega^2}{v^2} - H\right)X + 2\alpha\frac{\omega}{v}R + \frac{\omega}{v^2\epsilon} = 0 \tag{12}$$

where

$$v = \sqrt{v_{ns}v_{ps}}, \qquad \alpha = \frac{\alpha_n v_{ns} + \alpha_p v_{ps}}{2v} \tag{13}$$

$$r = \frac{v_{ns} - v_{ps}}{2v}, \quad H = \frac{J_{dc}}{v\epsilon}\left(2\frac{\delta\alpha}{\delta E} + y\frac{\delta}{\delta E}(\alpha_n - \alpha_p)\right) \tag{14}$$

$$Y = \frac{v\epsilon}{J_{dc}}\frac{\delta}{\delta x}E_m \quad \text{and} \quad E_m = E - \frac{q}{\epsilon}\int (N_D - N_A)\,dx \tag{15}$$

Here $\delta E_m/\delta x$ is the contribution by mobile space charge to the field gradient.

From the dc field and current profiles, the space-dependent quantities $\alpha_n(x)$, $\alpha_p(x)$, $\alpha(x)$, and $H(x)$ for a given doping profile and dc current density are evaluated and fed in as input data for small-signal analysis. The edges of the depletion layer of the diode, which are fixed by the dc analysis, are taken as the starting and the end points for small-signal analysis (21).

The boundary conditions for R and X are given by

$$\frac{\delta R}{\delta x} + \frac{\omega X}{v_{ns}} = -\frac{1}{v_{ns}\epsilon}, \qquad \frac{\delta X}{\delta x} - \frac{\omega R}{v_{ns}} = 0 \tag{16}$$

at the boundary of the n side, and

$$\frac{\delta R}{\delta x} - \frac{\omega X}{v_{ps}} = \frac{1}{v_{ps}\epsilon}, \qquad \frac{\delta X}{\delta x} + \frac{\omega R}{v_{ps}} = 0 \tag{17}$$

at the boundary of the p side.

An iterative computer simulation program which can iterate over initially chosen values of $R(x)$ and $X(x)$ is used to solve the differential equations with the given boundary conditions following a modified Runge–Kutta method (21).

The final solutions for the $R(x)$ and $X(x)$ profiles are then integrated to determine the total negative resistance Z_R and reactance Z_X of the diode. Thus

$$Z_R = \int_{-x_1}^{x_2} R\,dx \quad \text{and} \quad Z_X = \int_{-x_1}^{x_2} = X\,dx. \tag{18}$$

The diode impedance Z_d is given by $Z_d(\omega) = Z_R + jZ_X$, and the admittance Y_d is given by

$$Y_d = \frac{1}{Z} = \frac{1}{Z_R + jZ_x} = G + jB \tag{19}$$

The real and imaginary parts of the diode admittance can be computed for various dc current densities and for different frequencies to obtain G–B plots. The optimum frequencies for peak negative conductance and the avalanche frequency at which G becomes negative can be obtained from G–B plots. The small-signal G–B plots give the frequency range of operation of the device as well as the optimum values for the current density and the structural parameters for maximum output. The small-signal G–B plots are also the limiting conditions of large-signal G–B plots where the voltage amplitude tends to zero and give the preliminary design of a diode structure for operation within a given frequency range. The small-signal G–B plots for a Si X-band DDR for various current density will be discussed in connection with the effect of mobile space charge.

The plots of negative resistance in the depletion layer of IMPATT diodes show the relative contributions of various regions of the depletion layer to the high-frequency power (20). For double-drift diodes, $R(x)$ plots exhibit two maxima in the central part of the two-drift layer with a minimum in the avalanche layer very close to the junction. For silicon (in which $\alpha_n > \alpha_p$) DDR diodes, the maximum of $R(x)$ in the electron drift layer exceeds that in the hole drift layer in magnitude; the opposite is the case for GaAs (in which $\alpha_p > \alpha_n$) DDR diodes. It is also interesting to note that the avalanche region makes an appreciable contribution (though smaller than that of the drift region) to the high-frequency negative resistance.

The $R(x)$ profiles for silicon double-drift diodes for millimeter-wave frequencies of 60, 94, 140, and 220 GHz are shown in Fig. 12 for optimized current densities. Corresponding G–B plots, breakdown voltages, and avalanche- and drift-layer widths have been given by Pati et al. in Ref. 19.

LARGE-SIGNAL ANALYSIS OF IMPATT DIODES

Large-signal properties of IMPATT diodes were first studied by Evans and Haddad (22) using an analytical approach with simplifying assumptions. It was shown that the power output

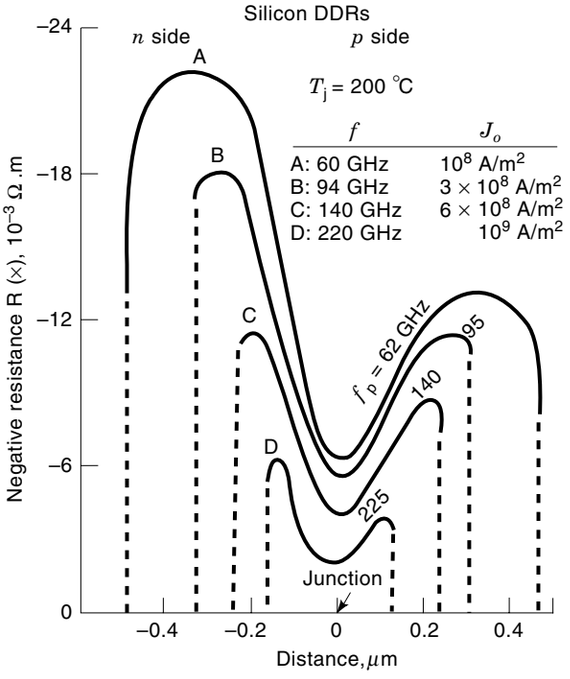

Figure 12. Space variation of diode negative resistance $R(x)$ in the depletion layer of silicon flat DDRs for various design frequencies at optimized current densities.

depends strongly on the series load resistance presented to the devices. When the ac voltage and carrier current have appreciable swings around dc values in each cycle, numerical solution of the Poisson and continuity equations is carried out by dividing the depletion layer width and the time period into a large number of space and time steps for accurate estimation of large-signal properties. The boundary condition of this complex problem is satisfied by a number of iterations taking into account the load impedance with which the device is terminated.

Scharfetter and Gummel (23), Chang and Hu (24), and Rolland et al. (25) carried out large-signal analysis of SDR and DDR IMPATTs and presented snapshots of the spatial profiles of electric field and carrier currents at quarter-period intervals within a time period. The profiles indicate that the position of the maximum electric field remains almost constant around the junction, while its magnitude undergoes periodic fluctuations. The carrier density buildup takes place during the second quarter period after the field maximum is reached at the end of the first quarter period. The electron and hole pulses are fully formed at the end of the second quarter period. These pulses travel towards both terminals during the next two quarter periods and are received there when the cycle is completed. The field then begins to rise in the charge-free depletion layer, and the cycle repeats.

Snapshots of an SDR large-signal oscillation are shown in Fig. 13, and the corresponding *G–B* plots are shown in Fig. 14. The peak negative conductance decreases with increase of voltage swing of the diode, thus giving a stable oscillation in the device when the impedance of the load matches that of the device.

DC-TO-MICROWAVE CONVERSION EFFICIENCY

The transit of carrier pulses in the drift region after avalanche buildup leads to a rectangular waveform of the current whose fundamental component is in antiphase with the sinusoidal voltage across the device. For full modulation, the fundamental component of the carrier current is given by $(4/\pi)I_0 \sin \omega t$. The dc-to-RF conversion efficiency of the device is thus given by the ratio of the output ac power to the input dc power,

$$\eta = \frac{P_{ac}}{P_{dc}} = \int_0^{2\pi/\omega} \frac{(4I_0/\pi)\sin\ \omega t \cdot V_m \sin\ \omega t\ dt}{I_0 V_0} = \frac{2}{\pi}\frac{V_m}{V_0} \quad (20)$$

where I_0 is the dc current, V_0 is the dc voltage, and V_m is the ac voltage magnitude. The maximum field swing E_m allowed in drift region of silicon diodes is assumed to be one-half the dc drift field E_d, so that the electric field in the drift region does not fall below that required for velocity saturation, i.e., $E_m = \frac{1}{2} E_d$. The magnitude of the ac voltage is approximately given by $V_{ac} = \frac{1}{2}(W_a + W_d) E_d$.

The efficiency of a silicon IMPATT diode for W_α small compared to W_d is given by Scharfeller and Gummel [23] as

$$\eta = \frac{2}{\pi}\frac{\left(\frac{1}{2}\right)V_D}{V_A + V_D} = \frac{1}{\pi}\frac{V_D}{V_A + V_D} = \frac{1}{\pi}\frac{1}{1 + V_A/V_D} \quad (21)$$

Thus to increase the conversion efficiency one needs to create a narrow avalanche region by appropriately tailoring the doping profile. For GaAs diodes, a much larger field swing is possible, as the velocity becomes saturated at a much lower field (10^5 V/m) than in silicon (2×10^6 V/m, which leads to a lower efficiency). It has been theoretically estimated that the maximum efficiency is 15%, 21%, and 38% for X-band SDR (Si), DDR (Si), and SDR (*n*-GaAs) respectively. The efficiency of 50 GHz Si DDR and SDR diodes has been measured and has been found to be 14 and 10%, respectively (26). For GaAs SDR diodes the measured efficiency ranges between 20 and 30% (27). For a more realistic calculation of the efficiency, one has to make a large-signal simulation of the device for different voltage swings and load impedances at various dc current densities. A calculation by Scharfetter and Gummel (23) for Read silicon diodes indicates efficiency variation from 5 to 15% for V_m varying from 10 to 30 V at a dc current density of 200 A/m^2.

EFFECT OF MOBILE SPACE CHARGE

The power output and efficiency of the IMPATT decrease with increase of dc current density when the flow of mobile charge distorts the electric field profile and expands the avalanche zone. The effect of mobile space charge and sharp expansion of the avalanche zone for silicon DDRs has been discussed by Sridharan and Roy (28) as shown in Figs. 15–17, for millimeter-wave Si IMPATTs by Roy et al. (21), and for GaAs and InP IMPATTs by Banerjee et al. (29). The dc results indicate that field profiles for flat-profile diodes get distorted and remain high over a wider portion of the depletion layer, as shown in Fig. 15 for X-band flat-profile Si DDR. This leads to an expansion of the central avalanche zone from 26% of the

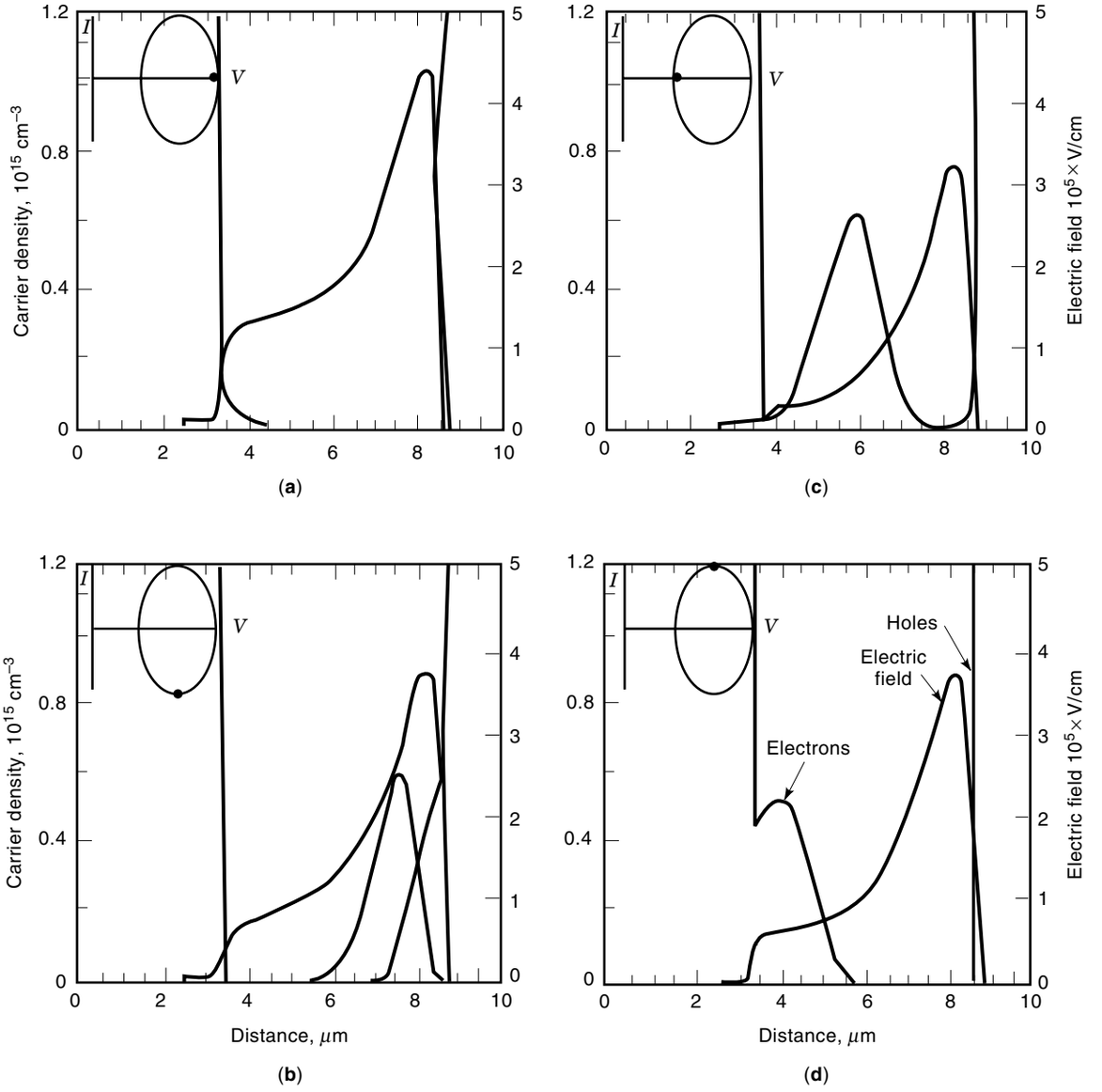

Figure 13. Profiles of hole and electron density and electric field at quarter-period intervals for a Read diode at a current density of 200 A/m^2 oscillating at 12.4 GHz. Terminal voltage and current indicated by phase plot. (Taken from Ref. 23 with permission from the IEEE.)

depletion layer at $J_0 = 10^7$ A/m^2 to 70% at the threshold of 10^8 A/m^2, when the avalanche zone sharply expands as indicated by the current profile in Fig. 16. This in turn leads to a sharp deterioration of dc-to-microwave conversion efficiency because of the decrease in drift zone widths on either side as indicated in Fig. 17.

The small-signal G–B plot of an X-band DDR has been presented by Sridharan and Roy (30) for various values of dc current density and is shown in Fig. 18. The small-signal analysis indicates that the magnitude of the maximum negative conductance initially increases with dc current but begins to decrease when the dc current exceeds the threshold value for sharp expansion of the central avalanche zone.

DOUBLE AVALANCHE REGION DIODE AND CANCELLATION OF SPACE CHARGE EFFECT

A *double avalanche region* (DAR) diode consists of two avalanche zones spaced by a drift zone and has a p^+nip^+ structure. This structure was first proposed by Som et al. (31). Accurate dc and small-signal analyses of it by Datta et al. (14) indicate that cancellation of mobile space charge effect takes place in the central drift region and the field profile is not affected at high dc current density (Fig. 19). The negative conductance occurs over several frequency bands and is unaffected by space charge, which may make this device suitable for high-power and high-frequency operation (31).

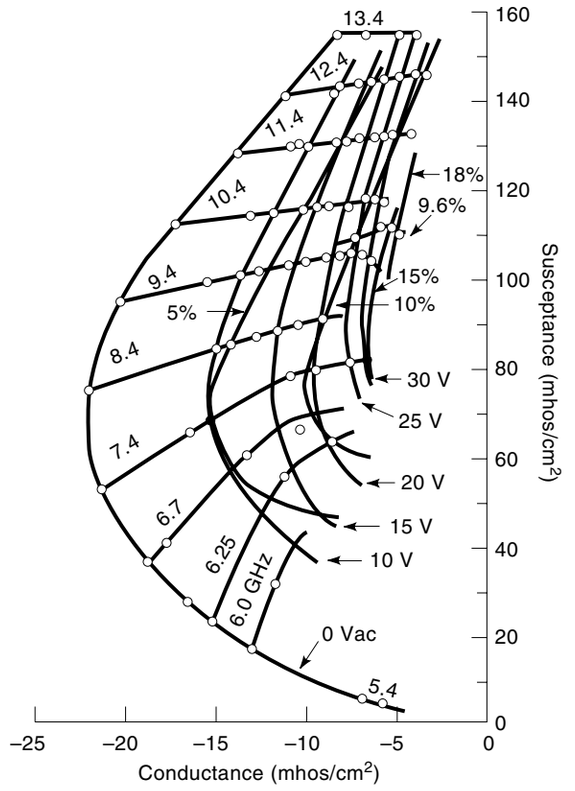

Figure 14. Large-signal admittance (susceptance versus conductance) of a Read diode for various frequencies and ac voltage amplitudes with corresponding efficiency at a current density of 200 A/cm^2. (Taken from Ref. 23 with permission from the IEEE.)

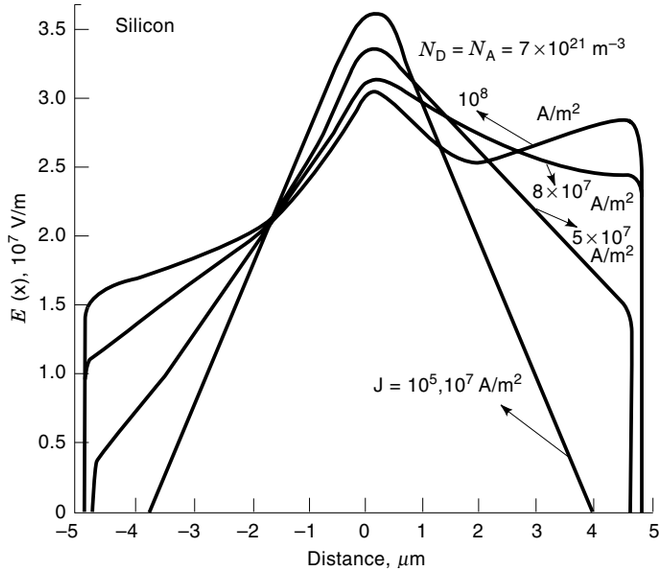

Figure 15. Electric field profiles of symmetrical double-drift region (n^+npp^+) silicon IMPATT for different values of dc current density.

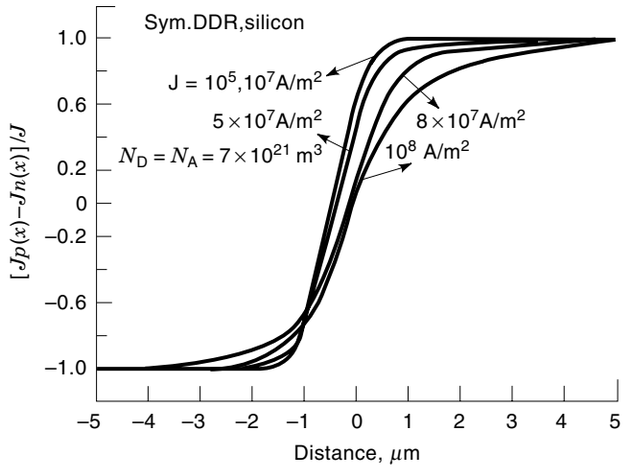

Figure 16. $[J_p(x) - J_n(x)]/J$ profiles of a symmetrical DDR silicon IMPATT for different values of dc current density.

LOW–HIGH–LOW DIODES FOR REDUCTION OF THE SPACE CHARGE EFFECT AND CONSTRICTION OF THE AVALANCHE ZONE

Low–high–low IMPATT diodes are emerging as more efficient devices than normal SDRs and DDRs. In such diodes impurity bumps of high doping density are incorporated by the MBE technique in appropriate positions of the flat-profile DDR or SDR, which decreases the effect of mobile space charge on the field profile in the drift zone and constricts the width of the avalanche zone, thereby increasing the efficiency of the device. Pulsed DLHL silicon devices have been shown to be capable of delivering large millimeter-wave power at 94 GHz at a dc current density of 10^9 A/m^2 (32).

HIGH-FREQUENCY CONSIDERATIONS

IMPATT diodes are the most powerful sources of millimeter-wave power, and IMPATT sources have been developed for atmospheric window frequencies of 35, 94, 140, and 220 GHz. As the frequency of IMPATT operation increases, the width of the depletion layer decreases, accompanied by a fall in breakdown voltage and power output. The maximum power output of an IMPATT diode falls off sharply at high frequencies due to limitations regarding the attainable impedance level in microwave circuit and the inherent limitations regarding the maximum electric field E_m at breakdown and the saturation drift velocity V_s. The maximum input power P_m is related to the frequency by

$$P_m f^2 = \frac{E_m^2 V_s^2}{8\pi X_C} \tag{22}$$

where $X_C = 1/2\pi fC$ and $C = \epsilon_s A/W$ is the capacitance of the depletion region. Thus the maximum input power decreases as $1/f^2$, which indicates the electronic limitation of power output at millimeter-wave frequencies. For the same circuit impedance, the output power from an oscillator decreases with increasing frequency as $1/f^2$. Higher breakdown voltage at the

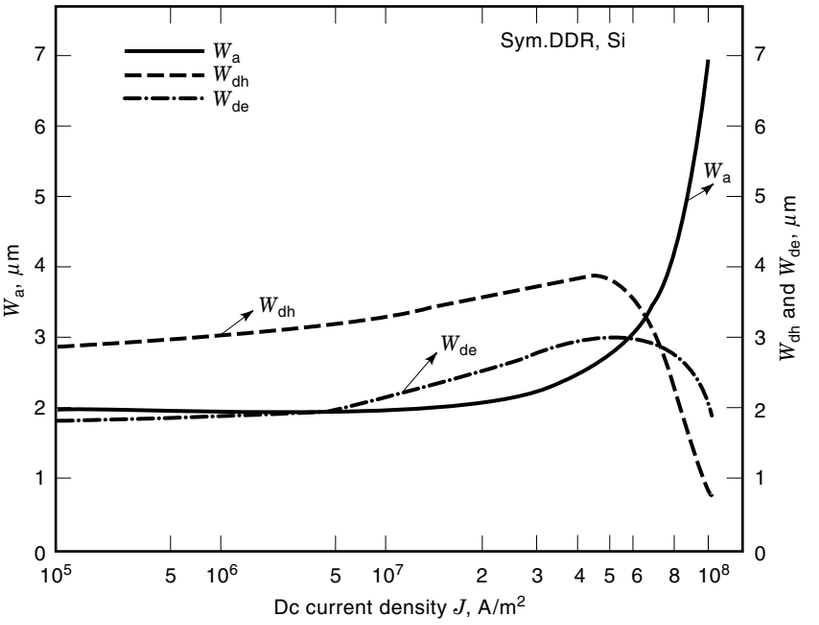

Figure 17. Plots of avalanche layer width W_a, electron drift region width W_{de}, and hole drift region width W_{dh} against dc current density.

same frequency of operation provides higher power output, and thus the DDR has an advantage over the SDR. InP, with a lower ionization rate than Si or GaAs for the same electric field, has higher breakdown voltage and should therefore be a suitable semiconductor for powerful millimeter-wave sources. But silicon remains the most important material for millimeter-wave IMPATTs because of its advanced technology and stability.

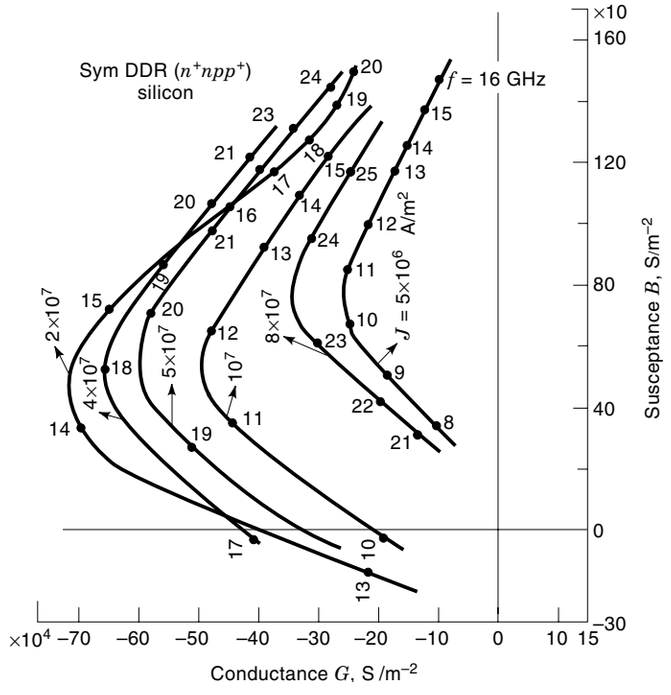

Figure 18. *G–B* plots of symmetrical double-drift silicon IMPATT diode for different values of dc current density.

At high frequencies (above 100 GHz), the value of the field maximum sharply increases, which in turn increases the possibility of tunneling across the junction. Elta and Hadded (33) suggested a mixed tunneling–avalanche transit time mode (MITTAT) and a tunnel transit time (TUNNETT) mode. Their calculations indicated that Si devices have higher tunneling frequency limit (≈400 GHz) than GaAs devices (≈75 GHz) and further that silicon devices between 400 and 500 GHz and GaAs devices between 75 and 150 GHz would operate in MITTAT mode.

At very high frequencies the depletion region of an IMPATT diode is very thin and the maximum electric field at breakdown becomes very high (>10^8 V/m). The ionization rates of charge carriers tend to saturate at very high field leading to a broadening of the injection current pulse. Also the tunneling becomes a significant process in addition to

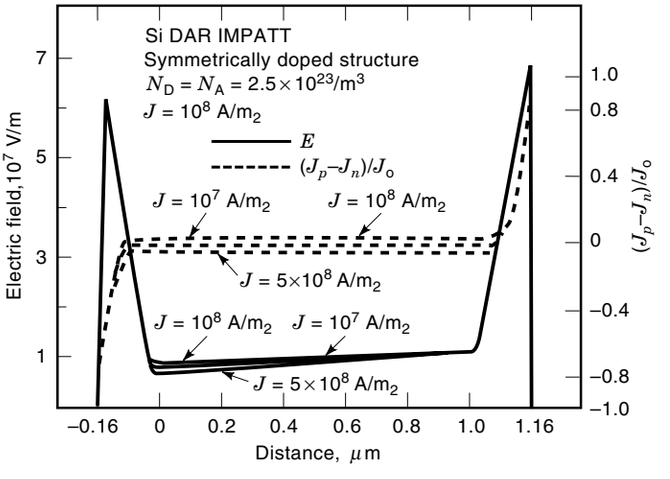

Figure 19. Field and carrier current profiles of symmetrically doped DAR IMPATT at various values of dc current density.

avalanche multiplication for very thin depletion layer, which leads to a change in the appropriate phase delay. Thus the saturation of ionization rates and the tunneling process reduce the power output of an IMPATT device at high frequency. Further, at very high frequencies the skin depth becomes smaller than the substrate dimensions and the current flow is confined within the substrate surface. Thus, the effective series resistance of the substrate is increased and the efficiency is reduced due to the skin effect. These fundamental limitations tend to sharply decrease the efficiency and power output of IMPATTs above 100 GHz.

Fabrication of IMPATT Diodes

Lower-frequency microwave (8–26 GHz) SDR diodes can be fabricated by diffusion technique. An epitaxial nn^+ silicon wafer with an n^+ high-conductivity (0.003 $\Omega \cdot$ cm) arsenic-doped substrate is subjected to boron diffusion at 1000–1200 °C to produce a p^+nn^+ structure. For X-band diodes the n layer is 4 μm thick. After diffusion, the wafer is vacuum-coated on the junction side, first with chromium and then with gold. Chromium prevents short-circuit breakdown by migration of gold atoms across the junction into the device at high temperature. The transition in the nn^+ layer has to be very sharp to reduce the positive parasitic resistance. For this, low-temperature epitaxial growth is required for the nn^+ epitaxial wafers. After vacuum coating at 10^{-8} mm Hg, the metallic layers are electroplated with gold to produce an integral heat sink of thickness around 200 μm. The substrate is then thinned to 10 μm by mechanical polishing and chemical etching. The substrate side is then vacuum-coated with chromium and gold. A photolithographic technique is then applied to define diodes with 100 μm diameter on an integral heatsink 500 μm square. After chip separation with a diamond scriber, each device is then encapsulated in a standard microwave package by die bonding and wire bonding. Fabrication process steps for X-band IMPATT diodes have been described in detail by Mitra et al. (34) and are shown in Fig. 20.

IMPATT chips in the microwave frequency range (<30 GHz) are packaged in standard microwave packages. The junction side of the chip is die-bonded to a gold-coated post of oxygen-free high-conductively copper in a bonding machine using heat, pressure, and ultrasonic vibrations. The metal cap on the other side of the package is isolated from the post by a ceramic cylinder. The other side of the chip is wire-bonded to the rim of the cap by means of gold wires [Fig. 22(a)].

NOISE IN IMPATT DIODES

The random process of avalanche multiplication and creation of electron–hole pairs in the avalanche zone of an IMPATT diode is the main source of noise in such devices. Avalanche multiplication not only multiplies the signal noise, but also adds a substantial amount of noise to it due to the statistical fluctuation of the multiplication factor. The noise at small signal level in silicon and GaAs diodes has been found to be 40 and 25 dB respectively. Silicon diodes have wider avalanche zones (since α_n is much greater than α_p) than GaAs diodes. GaAs diodes are thus less noisy, due to the smaller number of ionizing events in the narrow avalanche zone. The noise in avalanche transit time diodes has been thoroughly reviewed by Gupta (35).

THERMAL LIMITATIONS AND HEAT SINK

A large current flows through the active layer of an IMPATT diode: up to 10^7 A/m^2 for X-band diodes and up to 10^9 A/m^2 for W-band devices, with a breakdown voltage up to 80 and 20 V respectively. The power density is thus extremely high, ranging from 8×10^8 W/m^3 for X band to 2×10^{10} W/m^3 for W band. The continuous rise in temperature of the active region above ambient due to heat dissipation, without an appropriate heat sink arrangement, would cause the reverse saturation current to rise exponentially, leading to thermal burnout of the device. The temperature rise above the ambient should not be much above 100 °C, and an appropriate heat sink is essential for these devices. The most commonly used technique is to have an electroplated gold layer on the junction side of the wafer, of thickness 20 to 100 μm. For microwave diodes, the IMPATT chip is bonded to a gold-coated copper post of the package by thermocompression bonding. For millimeter-wave diodes, where heat dissipation is much larger, the copper heat sink is replaced by type II(a) diamond, which has a much larger thermal conductivity than copper (5 times as large) at room temperature. The device chip is bonded to the diamond heat sink by a bonding machine.

MILLIMETER-WAVE IMPATT DIODES

IMPATTs are now the most important solid-state sources of millimeter-wave power in the frequency range 30–300 GHz. From single flat-profile DDR device, CW powers of 1 W at 94 GHz and 50 mW at 220 GHz (36) have been obtained. Misawa and Marinaccio (37) obtained 74 mW with 3.2% efficiency at 110 GHz from an abrupt-junction silicon diode. A double-drift millimeter-wave silicon diode was first reported by Seidel et al. (26), who obtained 1 W at 50 GHz with 14% efficiency. Ishibashi et al. (2) obtained 2.2 mW from SDR silicon diodes at very high frequency of 412 GHz and highest IMPATT oscillation was reported to be 430 GHz.

In recent years, the molecular-beam epitaxy (MBE) technique has been increasingly used for IMPATT fabrication; by that means very thin layers of appropriate doping can be grown to realize flat and low–high–low DDR doping profiles. Luy et al. (38) obtained CW power of 600 mW at 94 GHz with 6.7% efficiency from MBE-grown flat-profile DDR. Important points concerning millimeter-wave DDR fabrication will now be outlined.

Junction Formation

The silicon DDR is the preferred structure for millimeter waves. For fabrication of p^+pnn^+ devices, n and p layers are epitaxially grown to the designed thickness on an n^+ arsenic-doped low-resistivity (0.003 $\Omega \cdot$ cm) silicon substrate. Using boron diffusion, a p^+ layer is formed on the p side to provide contact for the DDR. Ion implantation is also used to fabricate millimeter-wave DDRs by multiple-energy ion implantation to overcompensate a fraction of the n side grown epitaxially on the n^+ substrate so as to form a pnn^+ structure. Boron diffusion is then used to form the contact p^+ layer on the p layer formed by ion implantation, to obtain the DDR device with p^+pnn^+ structure.

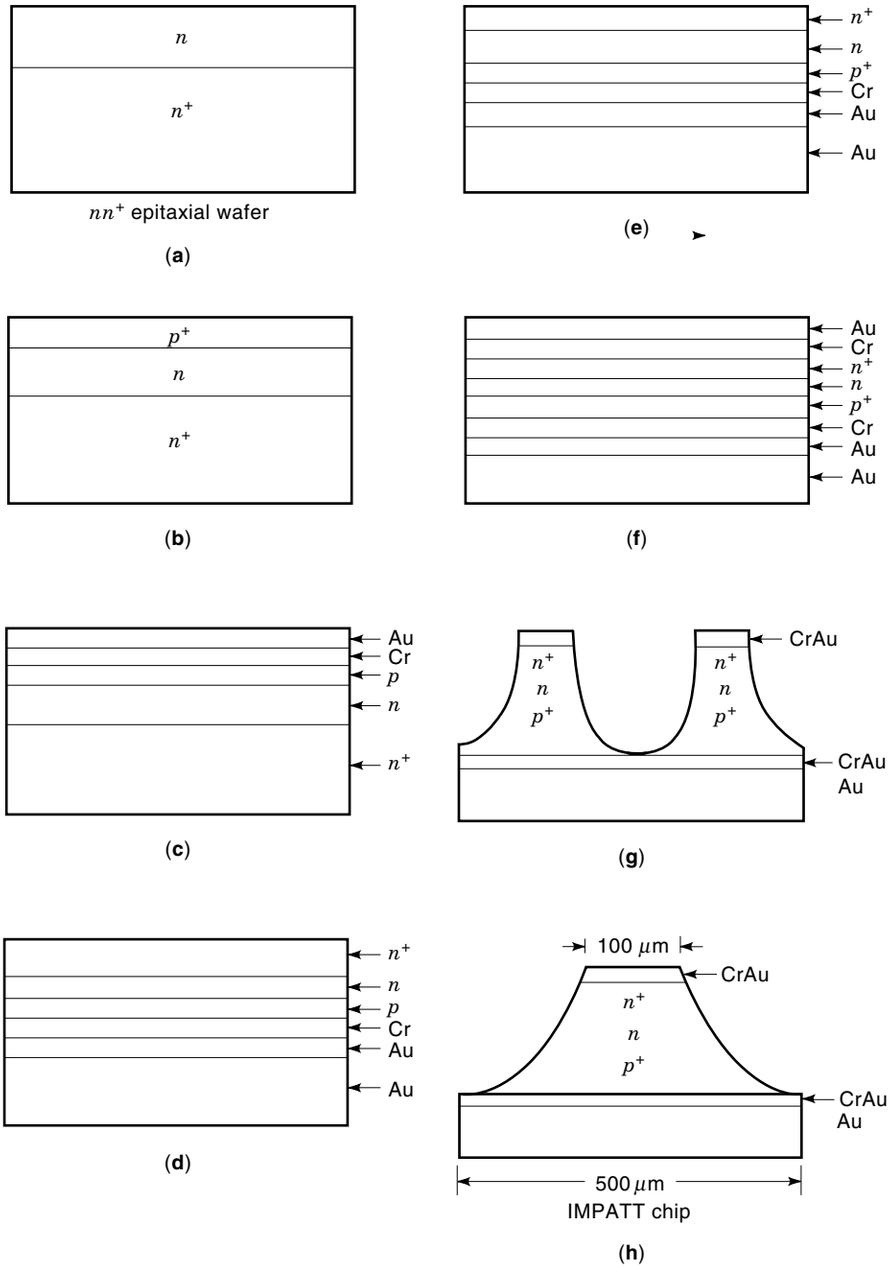

Figure 20. Fabricational process steps for X-band Si IMPATT diode: (a) epitaxial wafer; (b) after boron diffusion; (c) after vacuum coating by Cr and Au; (d) after electroplating of Au; (e) after thinning of substrate; (f) after vacuum coating of Cr and Au on n^+ side; (g) after photolithography and mesa etching; (h) after chip separation.

It has already been stated that molecular beam epitaxy is being used to realize thin layers of appropriate doping for millimeter-wave IMPATT diodes. Due to relatively low temperature of the epitaxial process, a steep transition in doping concentration can be achieved, and precise control of thickness and doping can be realized by the MBE technique, which is now being used for fabrication of millimeter- and sub-millimeter-wave IMPATTs, both SDR and DDR. At very high frequencies SDR silicon diodes are preferred for their simplicity of fabrication. Various experimental reports are available on fabrication of silicon SDRs in the frequency range 30–300 GHz, showing good performance with regard to power output and efficiency.

Series Resistance

Reduction of the positive series resistance is extremely important for millimeter-wave IMPATTs. For this purpose the device substrate has to be made as thin as possible by chemical etching. Typically a substrate for 35 GHz has to be thinned to 20 μm; for frequencies above 100 GHz it has to be thinned to 5 μm or less.

Metallization

Contact metallization is very important in the fabrication of millimeter-wave IMPATTs, in view of their large current density (10^8 to 10^9 A/m^2) and small junction area (diameter 10 to

30 μm). A three-component contact metallization is used with 600 Å of chromium, a platinum barrier layer of 2000 Å thickness, and an evaporated gold layer of 3000 Å, followed by 3 μm of electroplated gold. The evaporation has to be done in ultrahigh vacuum for good contact.

Millimeter-Wave IMPATT Packaging

Between 30 and 100 GHz the device chip is usually bonded to a selectively metallized diamond heat sink, which has a high thermal conductivity, for flow of heat from the junction to the ambient. The heat sink is sealed in a quartz ring with a number of gold ribbons bonded to the device and the top metal cap (36) as shown in Fig. 21(a). For frequencies higher than 100 GHz a single- for double-metallized quartz standoff mounting arrangement is used as shown in Fig. 21(a) and Fig. 22 to reduce the shunt capacitance to 0.01 pF, which is sufficiently small for operation up to 200 GHz. A direct contact method in which a thin bias pin makes contact with diode chip has been adopted at 100 GHz by Misawa and Marinaccio (37). At higher frequencies a direct contact method has been adopted (Fig. 22), which makes use of a wire welded on the tip of the bias pin to contact the IMPATT chip (39). Copper and diamond are both used as heat sinks for millimeter-wave chips. But for high current density and CW operation, diamond is preferred, because its thermal conductivity is 3 to 5 times larger than that of copper between 500 and 300 K.

PULSED MILLIMETER-WAVE IMPATT DIODE

Pulsed millimeter-wave IMPATT diodes are becoming important in solid-state transmitters for radar systems, missile seekers, etc. Pulse powers of 23 W at 35 GHz, 15 W at 94 GHz, and 3 W at 140 GHz have been reported (40). Experimental reports of higher pulsed power output (42 W at 94 GHz) have since been presented (41) for a DDR device fabricated by MBE.

The current density in pulsed diodes can be made much larger than that for CW device for realizing high output power, since the thermal dissipation is much lower for a short pulse duration. However, with increasing current density the electric field profile becomes distorted by the mobile space charge, which leads to expansion of the central avalanche zone and reduction of the conversion efficiency. Design of pulse IMPATT diodes must therefore take into consideration the space charge effect at high current density. Computer studies have been made on DDR designs (32) to constrict the avalanche zone and increase the width of the drift zones by incorporating single or double impurity bumps on either side of the DDR junction. Figures 23 and 24 show the doping and field profiles for optimized double low–high–low (DLHL), single low–high–low (SLHL), and flat-profile DDRs for operation at 94 GHz. It is seen from the field profiles that the bumps prevent the expansion of the avalanche zone for DLHL for current densities as high as 10^9 A/m^2. From the small-signal conductance–susceptance (G–B) plots in Fig. 25, it is seen that the highest negative conductance is exhibited by DLHL, followed by SLHL and flat DDR, in the W band. This is due to the reduction of space charge effects in DLHL. Studies on the optimization of the bump positions, the bump height, and the bump shape have been made (32), which show that the negative conductance decreases for DLHL and SLHL structures as the bumps shapes change from ideal rectangular to the more realistic trapezoidal.

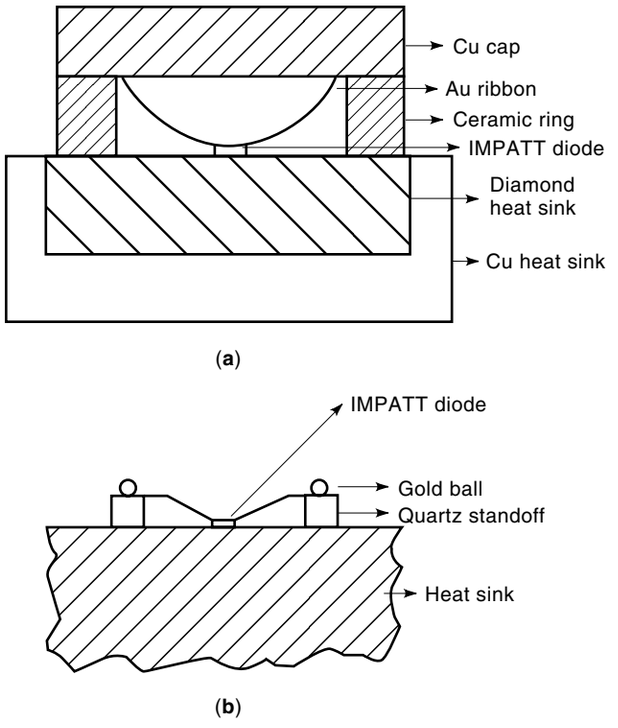

Figure 21. Millimeter-wave diode package: (a) ceramic ring; (b) double quartz standoff. (After Ref. 36.)

FREQUENCY CHIRP IN PULSED IMPATT OSCILLATORS

The temperature of an IMPATT junction increases with time during the short current pulse, which leads to a change in frequency during the pulse period due to the variation of diode impedance.

For a flat current pulse the oscillation frequency decreases due to rise in temperature. Since frequency increases with bias current, the slope of the bias current pulse can be made positive and its value can be suitably adjusted so that the thermal and bias current effects may cancel each other, leading to zero chirp (39).

GaAs AND InP IMPATT DIODES

GaAs has emerged as a highly suitable semiconductor for IMPATTs in the lower microwave frequency range, where the efficiency of GaAs device has exceeded that of silicon devices. Goldwasser and Rosztoczy (42) reported high-efficiency GaAs low–high–low SDR diodes delivering 2.9 W with 35.6% efficiency at X band. Iglesius et al. (1) reported 12.5 W output at 6.1 GHz with 26.6% efficiency for SDR Schottky barrier high–low GaAs diodes. Alderstein et al. (43) reported 710 mW output for a GaAs Read diode with 9% efficiency in the 36–38 GHz range. Vasudev (44) reported 40 W of pulsed power from GaAs double drift IMPATTs at 9.4 GHz with 10% efficiency. At higher frequencies the power output of GaAs diodes is very low. Chang et al. (45) reported fabrication of a Read type

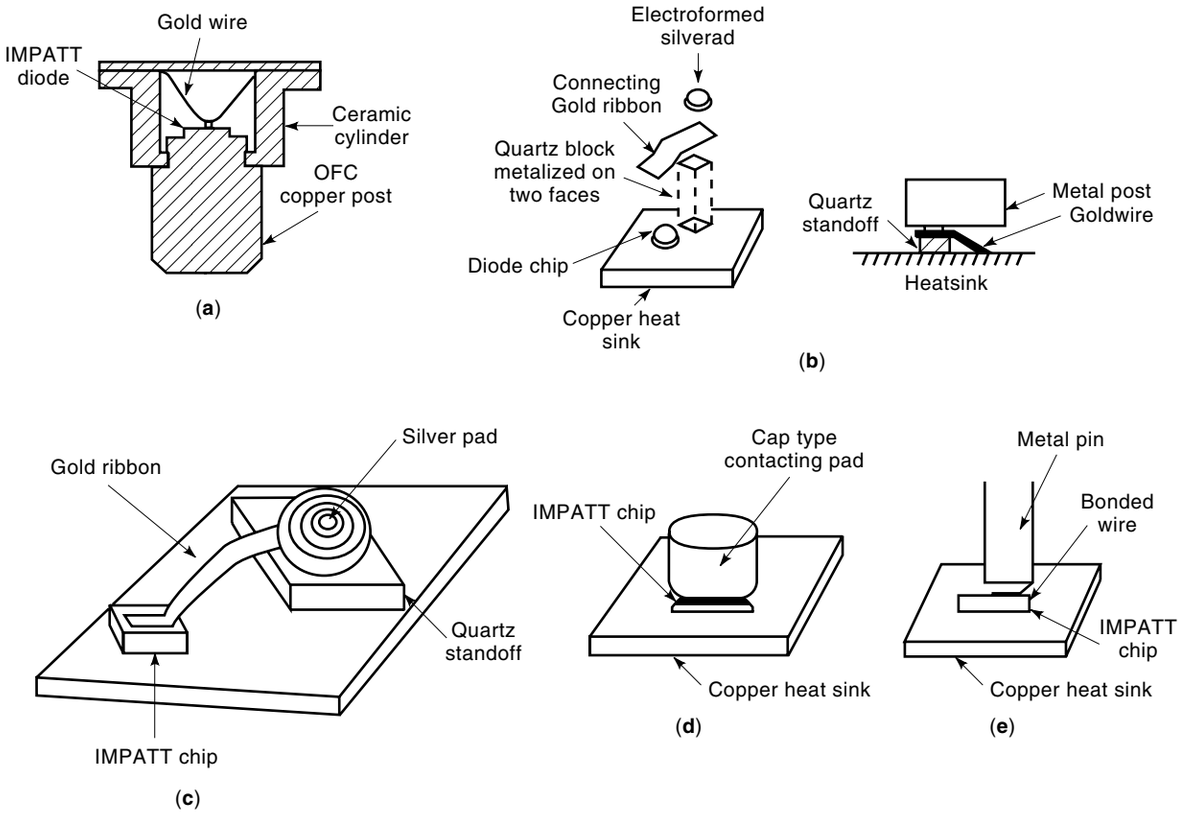

Figure 22. Packaging and bonding arrangements for IMPATT diodes: (a) microwave diode up to 30 GHz; (b)–(e) millimeter-wave diodes above 100 GHz. (After Refs. 36 and 39 with permission from the IEEE.)

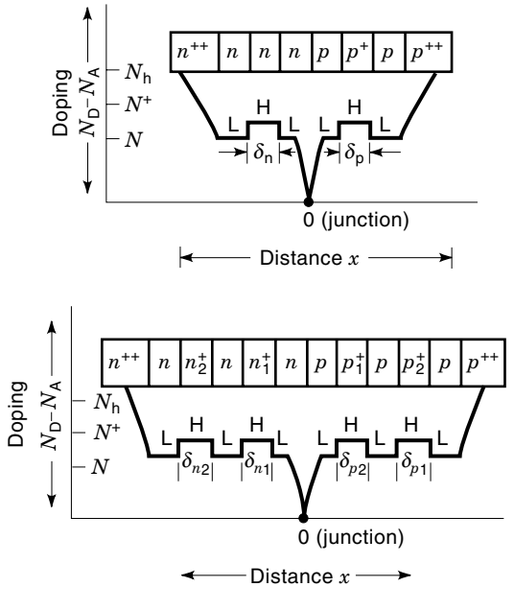

Figure 23. Schematic diode structure and doping profile of SLHL and DLHL DDR IMPATT diodes.

GaAs IMPATT diode by VPE and obtained CW power of 5 mW with 0.5% conversion efficiency at 130 GHz. It can be stated that GaAs high–low and low–high–low diodes exhibit higher efficiency than any other IMPATT below 30 GHz.

The fabrication of ion-implanted single-drift flat-profile p^+nn^+ InP IMPATT diodes operating at X band was reported

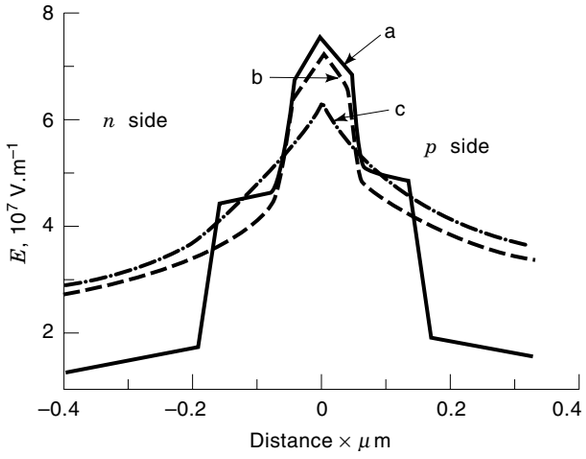

Figure 24. Field profiles of millimeter-wave silicon (a) DLHL, (b) SLHL, and (c) flat-profile DDR IMPATT diodes ($J = 1 \times 10^9$ A/m^2, $T = 673$ K).

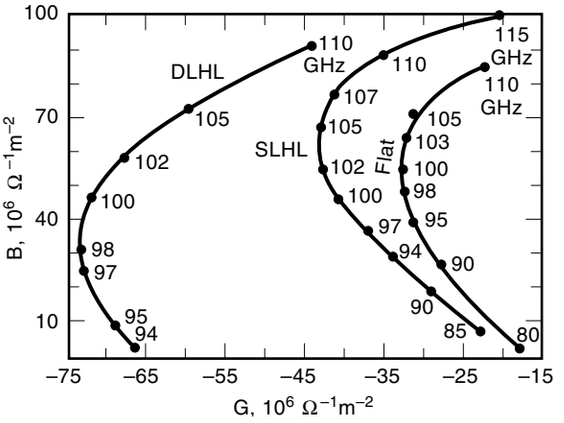

Figure 25. *G–B* plots of millimeter-wave silicon DLHL, SLHL, and flat DDR diodes at $J = 1 \times 10^9$ A/m^2 and $T = 673$ K.

by Berenz et al. (46) in 1978. Singly ionized Be ions with 50 keV energy were implanted into *n*-type InP epitaxial layers with sulfur as the chemical impurity on a tin-doped ⟨100⟩-oriented substrate grown by vapor phase epitaxy. The diodes exhibited CW output power of 1.6 W with 11.1% efficiency at 9.78 GHz. In low-duty-cycle pulse operation 6.1 W peak output power was achieved at 10.8 GHz with 13.7% efficiency.

Computer studies with ionization data of Ito et al. (10) for GaAs were carried out by Banerjee (47) on GaAs, SDR, DDR, and low–high–low diodes by the methods outlined earlier. Similar computer studies have been carried out by Banerjee for InP diodes (47). The results indicate that GaAs diodes should exhibit higher efficiency than silicon due to the narrower avalanche zone at microwave frequencies. The InP diode should have higher breakdown voltage at millimeter-wave frequencies due to lower values of the ionization rate and should deliver higher power at those frequencies. GaAs diodes should surpass silicon devices in the lower microwave range (6–30 GHz), and InP diodes have great promise in the field of millimeter waves. But silicon devices are more stable and reliable and are based on a more mature technology, and should therefore dominate as premier solid-state sources for millimeter and submillimeter waves in the foreseeable future.

HETEROJUNCTION IMPATT DIODES

Heterojunction IMPATTs based on GaAs/Al_9Ga_7As have been reported in recent years (48) which indicate significant improvements in performance over conventional GaAs *pn* junctions. The devices were grown using MBE technique and show 2 to 3 orders less magnitude of leakage current prior to avalanche breakdown and 2 dB power improvement at Ku Band. The small leakage current and sharp avalanche breakdown lead to generation of sharp pulses in each cycle in the heterojunction device, causing increased RF power and reduced phase noise.

CONTROL OF IMPATT PROPERTIES BY OPTICAL ILLUMINATION OF THE ACTIVE AREA AND BY A TRANSVERSE FIELD IN THE DRIFT REGION

Optical illumination of an IMPATT device enhances the leakage current entering the depletion layer and decreases the current multiplication factor of electrons and holes. It has been shown theoretically for Read as well as double-drift diodes (49,50) that a decrease in current multiplication factor will lead to an increase in optimum frequency for oscillation, since the avalanche time delay will be shorter, and to a decrease in the magnitude of the negative conductance and the output power. Experimentally, Cottrell et al. (51) and Vyas (52) have observed an increase in the frequency of oscillation by 10 MHz and a decrease in power output by 10% for X-band devices upon illumination of the IMPATT active area. Vyas et al. (53) have considered two mounts—*flip chip* and *top-mounted* (Fig. 26)—for optical illumination experiments and have shown that electron leakage current is more effective than hole leakage current in producing a change of the oscillation frequency. Mazumder and Roy (54) extended computer studies in the millimeter-wave range to the W band and found that a large shift in the oscillation frequency can be obtained by increasing the leakage current through optical illumination for low–high–low DDR silicon and GaAs diodes.

Seeds and Forrest (55) reported optical injection locking of IMPATT oscillators by illuminating the unpackaged IMPATT device in a microstrip oscillator circuit with a laser beam amplitude-modulated at a microwave frequency; they obtained a locking range of 1 MHz. Since then, a large number of investigations have been carried out on optical injection locking of IMPATTs by shining laser beams on IMPATT chips.

It has been shown that the frequency of an IMPATT can be controlled by the application of a field in the drift region transverse to the junction field (56). This effectively increases the transit time delay, since the direction of the drift velocity

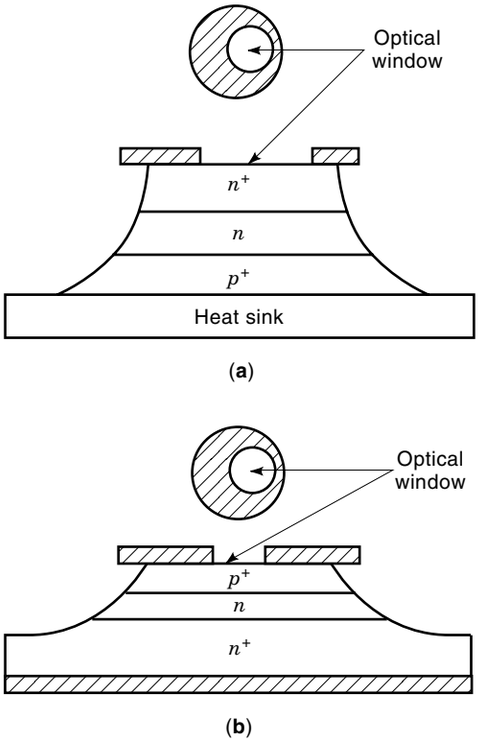

Figure 26. (a) Flip chip and (b) top-mounted SDR diodes with optical windows.

of the carriers changes while the magnitude remains saturated, and the carriers require more time to cross the drift layer.

TRAPATT DIODE

The acronym TRAPATT stands for *trapped plasma avalanche triggered transit,* which indicates the physics of TRAPATT diode operation. It is a solid-state microwave device with very high dc-to-microwave conversion efficiency (50–60%), capable of producing high power in pulsed operation. TRAPATT operation was first reported in 1967 by Prager, Chang, and Weisbroad (57). Basically it is a reverse-biased p^+nn^+ or n^+pp^+ junction with high punchthrough, i.e., the electric field is considerable on the lightly doped side of the nn^+ or pp^+ transition, but abruptly becomes zero on the substrate side. The frequency range of these devices is inherently limited to lower microwave frequencies, and the noise is larger than that in IMPATTs, although power output and conversion efficiency are both high.

Computer simulation of the device (58,59) has established that a transient avalanche zone is generated at the p^+n or n^+p junction by a trigger pulse, which propagates like a shock front through the depletion layer and fills it with a dense plasma of electrons and holes. The plasma thus formed causes a sharp decrease of the electric field behind the avalanche shock front, which propagates from the junction end to the other end of the depletion layer. The collapse of the electric field leads to the trapping of the plasma, and the electrons and holes now move towards the two ends with a much-reduced plasma velocity determined by the low-field mobility.

The field recovers slowly at first as the trapped carriers get out of the depletion layer with low plasma velocity, and then rapidly as the remaining carriers leave the depletion layer with saturated velocity due to the rise of field with the extraction of the plasma. The device thus oscillates between a high-current low-voltage state and a high-voltage low-current state after full recovery of the electric field in each cycle (60).

The propagation of the avalanche zone and formation of the electron–hole plasma is shown in Fig. 27 at several instants T_1, T_2, T_3, T_4 immediately after the device is suddenly subjected to a voltage greater than that for dc breakdown. A very high displacement current J flows through the depletion layer at time T_1, which produces an upward shift of the field curve, since

$$J = \epsilon_s \frac{\Delta E}{\Delta t} \tag{23}$$

and increases the field above the dc breakdown value. This leads to the formation of the electron–hole plasma at time T_2. The spatial slope of the field in the depletion layer in front of the plasma is determined by the doping density and is given by the Poisson equation,

$$\frac{\Delta E}{\Delta x} = \frac{q}{\epsilon_s} N_D \tag{24}$$

where q is the electronic charge, ϵ_s is the semiconductor permittivity, and N_D is the doping density of the n region.

The electric field variation in time and space in front of the plasma is given by Eqs. (23) and (24). Hence the velocity v_z of the avalanche shock front is given by

$$v_z = \frac{\Delta x}{\Delta t} = \frac{\Delta E/\Delta t}{\Delta E/\Delta x} = \frac{J}{qN_D} \tag{25}$$

For typical TRAPATT oscillator v_z is about 3 times the saturated drift velocity v_s.

After the formation of trapped plasma, the depletion layer is filled with a dense plasma of electrons and holes, and the electric field is low, as shown in Fig. 27. Electrons and holes begin to flow towards the positive and negative terminals with low velocity μE, where μ is the low-field mobility and E is the low field in the plasma. The initial slow recovery, as shown in Fig. 27, indicates that the central region still contains electron–hole plasma, whereas on either side only electrons or only holes are flowing towards the terminals and the electric field is rising due to the extraction of charge. The field recovers then to a higher value as shown in Fig. 28(e), and the remaining carriers are swept out of the active region, leading to a fast recovery of the electric field. The process repeats, leading to the voltage and current waveforms shown in Fig. 27(b) and 27(a).

A triggering pulse is needed to provide the necessary overvoltage to drive the device into the trapped plasma state in each TRAPTT cycle. This is provided by slug tuners in front of the device, mounted at the end of a coaxial line. Whenever a diode is driven to trapped plasma, the voltage across it suddenly falls. The resulting negative voltage pulse is propagated along the transmission line and gets reflected from the nearest tuner, placed half a wavelength away from the diode. The return pulse changes sign and arrives one pulse after the original pulse to provide the trigger to the diode for the next trapped plasma state.

It has been found that a punchthrough diode is essential for TRAPTT operation. The width W of the active region of doping N_A must be lower than $W_B = \epsilon E_B/qN_A$, the depletion layer width of the nonpunchthrough abrupt junction diode with breakdown field E_B at one edge. The punchthrough factor $F = W/W_B$ is 2 for typical TRAPATT operation.

The sum of the shock front period and the recovery period is approximately half the total period, so that the frequency of the TRAPATT operation is given by

$$f = \frac{1}{2T} \qquad \text{where} \quad T = \frac{W}{v_z} + \frac{W}{2}\left(\frac{1}{v_p} + \frac{1}{v_s}\right) \tag{26}$$

The low value of the plasma velocity v_p limits the operation of TRAPATT to the lower microwave frequency range. In practice, most of the experimental reports on TRAPATT oscillators are in the frequency range 0.5 to 10 GHz. Thus 1.2 kW output in the pulse mode has been obtained at 1.1 GHz by Liu and Risko (61) with an efficiency of 60%, and peak powers of 100 to 50 W have been obtained in the frequency range 4 to 8 GHz.

BARITT DIODES

The BARITT (an acronym for *barrier injection transit time*) is a transit time diode that generates power with low noise at microwave frequencies. It has normally a p^+np^+ or metal–n–metal (mnm) structure and is equivalent to a pair of diodes connected back to back, one of which is forward-biased and

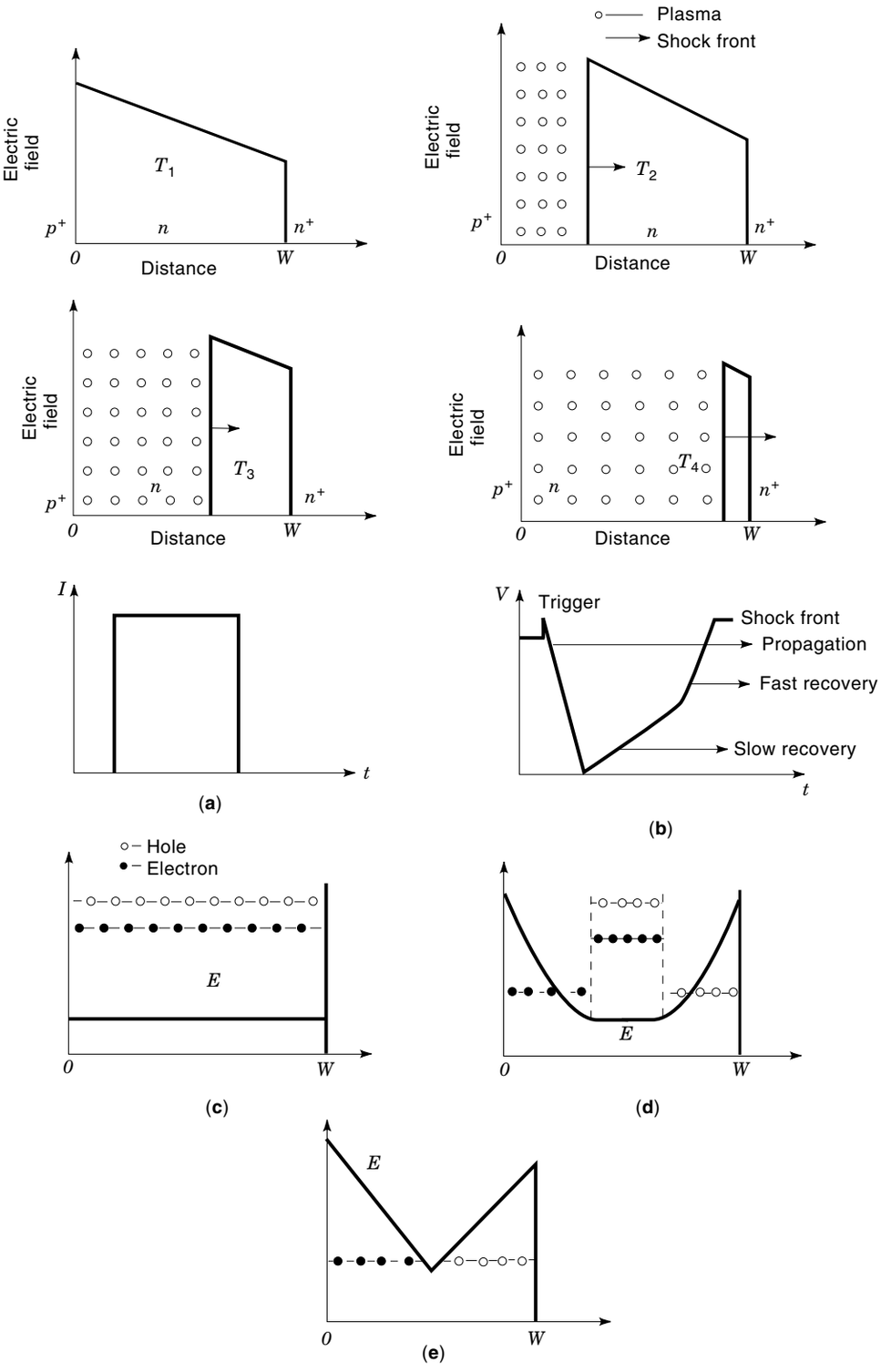

Figure 27. TRAPATT diode. Propagation of avalanche zone and formation of e–h plasma, at different instants of time $T_1 < T_2 < T_3 < T_4$: (a) current and (b) voltage waveforms; (c), (d) slow recovery of electric field; (e) fast recovery of electric field. (After Ref. 60.)

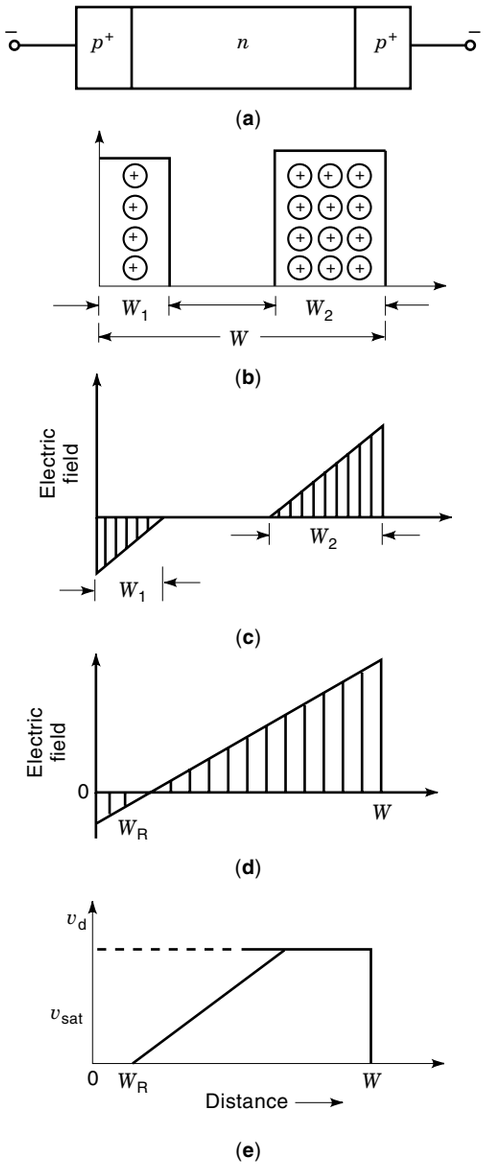

Figure 28. BARITT diode: (a) p^+np^+ BARITT structure; (b) low-bias charge distribution; (c) field distribution at low bias; (d) field distribution after reachthrough; (e) drift velocity distribution after reachthrough. (After Ref. 64 with permission from Elsevier Science Ltd.)

the other reverse-biased. Microwave oscillation in *mnm* BARITT diodes was reported by Colman and Sze (62) and Sze et al. (63) and in p^+np^+ BARITT diodes by Chu and Sze (64). When the depletion layer of the reverse-biased junction reaches that of the forward-biased junction, thermionic injection of minority carriers into the central n region takes place across the barrier of the forward-biased junction. The injected carriers are swept through the depletion layer by the reverse field to the other terminal. The transit time of charge carriers tends to be higher in BARITT structures because of the low-field part of the n region, which limits the frequency range of BARITT operation. BARITT operation for *mnm* structures has been observed at 4–8 GHz.

The p^+np^+ BARITT structure is shown in Fig. 28 together with the dc field profile at low bias and at the reachthrough voltage when the depletion region of the reverse-biased junction just reaches that of the forward-biased junction. The widths of the junctions are given by

$$w_1 = \sqrt{\frac{2\epsilon_s}{qN_D}(V_{bi} - V_1)} \tag{27}$$

for the forward-biased junction and

$$w_2 = \sqrt{\frac{2\epsilon_a}{qN_D}(V_{bi} + V_2)} \tag{28}$$

for the reverse-biased junction, where V_{bi} is the built-in voltage, V_1 is the portion of the applied voltage across the forward-biased junction, and V_2 is the portion of the applied voltage across the reverse-biased junction.

At reachthrough, $w_1 + w_2 = w$ and

$$V_{RT} = \frac{qN_D}{2\epsilon_s}w^2 - w\left(\frac{qN_DV_{bi}}{\epsilon_s}\right)^{1/2} \tag{29}$$

After reachthrough the hole current is thermionically emitted over the barrier, and for $V > V_{RT}$, the current increases exponentially with voltage. The transit time of injected carriers for crossing in the drift region is given by

$$\begin{aligned} T_d &= \int_{x_R}^{\alpha} \frac{dx}{\mu_n E(x)} + \int_{\alpha}^{w} \frac{dx}{v_s} \\ &= \frac{\epsilon_s}{q_nN_D}\int_{x_R}^{a} \frac{dx}{x} + \frac{w-a}{v_s} \end{aligned} \tag{30}$$

Carriers are injected at a phase angle of approximately $\pi/2$, when the ac field reaches its maximum, and the carrier current reaches the terminal after $\frac{3}{4}$ of the time period for optimum operation. Thus $T_d = \frac{3}{4}T = 3/4f$, and the frequency of oscillation can be written as

$$f = \frac{3}{4T_d} \approx \frac{3}{4}\quad\frac{v_s}{w} \tag{31}$$

A detailed study of the small-signal impedance of p^+np^+ BARITTs has been carried out by Weissglas (65) with current density as parameter. The result indicates that the peak negative resistance reaches its maximum value at a rather low dc current of 50 A/cm^2 for an n-region length of 7 μm and then decrease at higher dc current densities. The resistance of the forward-biased p^+n junction decreases with increasing dc current and tends to short-circuit the junction capacitively at high current. Thus the high-frequency negative resistance begins to decrease at lower current levels for BARITT structures, which leads to low output power and low efficiency.

Microwave power has been observed for BARITT structures in the frequency range 4 to 8 GHz. The power output varied from 2 to 8 mW for the initial *mnm* diodes reported by Coleman and Sze operating between 4 and 6 GHz.

An output power of 152 mW has been observed in Pt Schottky BARITT diodes at 8.6 GHz with a peak efficiency of 2.3% (66).

Unlike the IMPATT, the BARITT is a low-noise device, since no random avalanche multiplication is involved in it. The noise arises only from the shot noise of injected carriers due to the random fluctuations of the velocity of the carriers in the drift zone. An experimentally measured noise figure of 10 to 14 dB has been observed in a Si BARITT diode for a current density of 17 A/cm^2 around 7 GHz.

In BARITTs the field is low over a considerable fraction of the drift region where the carriers move with nonsaturated drift velocity determined by the low field mobility. Thus the transit time is high and the field swing is limited, leading to low frequency and low power output for BARITTs.

In conclusion, it may be stated that the BARITT is a transit time device with good noise performance, but it can operate only below X band and can deliver only small output power, with low efficiency.

ACKNOWLEDGEMENT

The author wishes to acknowledge the kind assistance received from the research associates Dr. Nilratan Mazumder and Dr. Dibyendu Ghoshal and from the research fellow Mr. Pankaj De. He also wishes to thank Mrs. Rama Chakraborty for her conscientious computer typing of the manuscript. The author wishes to express his gratitude to the Centre of Advanced Study in Radio Physics & Electronics, Calcutta University, for providing the necessary facility and environment for carrying out this work.

BIBLIOGRAPHY

1. D. E. Iglesias, J. C. Irvin, and W. C. Niehaus, 10 W and 12 W GaAs Impatts, *IEEE Trans. Electron Devices,* **ED-22**: 200, 1975.
2. T. Ishibashi et al., Liquid-nitrogen cooled submillimeter wave silicon IMPATT diodes, *Electron. Lett.,* **13**: 299–300, 1977.
3. R. B. Johnston, B. C. Deloach, and B. G. Cohen, A silicon diode microwave oscillator, *Bell Syst. Tech. J.,* **44**: 369–372, 1965.
4. W. T. Read, A proposed high frequency negative resistance diode, *Bell Syst. Tech. J.,* **37**: 401–446, 1958.
5. C. Canali, G. Ottaviani, and A. A. Quaranta, Drift velocity of electrons and holes and associated anisotropic effects in silicon, *J. Phys. Chem. Solids,* **32**: 1707, 1971.
6. P. A. Houston and A. G. R. Evans, Electron drift velocity in *n*-GaAs at high electric field, *Solid State Electron.,* **20**: 197–204, 1977.
7. V. B. Dalal, Hole velocity in *p*-GaAs, *Appl. Phys. Lett.,* **16**: 489–491, 1970.
8. R. E. Levinshtein, Recent results of studies of intervalley transfer of hot electrons, *Sov. Phys. Semicond.,* **13**: 735–745, 1979.
9. L. W. Cook, G. E. Bulman, and G. E. Stillman, Electron and hole impact ionisation coefficients in InP determined by photomultiplication measurements, *Appl. Phys. Lett.,* **40**: 589–591, 1982.
10. M. Ito et al., Ionization rates for electrons and holes in GaAs, *J. Appl. Phys.,* **49**: 4607–4608, 1978.
11. W. N. Grant, Electron and hole ionization rates in epitaxial silicon at high electric field, *Solid State Electron.,* **16**: 1189–1203, 1975.
12. R. A. Logan and S. M. Sze, Avalanche multiplication in Ge and GaAs *p–n* junctions, *J. Phys. Soc. (Japan) Suppl.,* **21**: 434, 1966.
13. S. M. Sze and G. Gibbons, Avalanche breakdown voltage of abrupt and linearly graded *p–n* junction in Ge, Si, GaAs and GaP, *Appl. Phys. Lett.,* **8**: 111, 1966.
14. D. N. Datta et al., Computer analysis of dc field and current density profiles of DAR Impatt diode, *IEEE Trans. Electron Devices,* **ED-29**: 1813–1816, 1982.
15. M. Gilden and M. E. Hines, Electronic tuning effects in the Read microwave avalanche diodes, *IEEE Trans. Electron Devices,* **ED-13**: 169–175, 1966.
16. T. Misawa, Negative resistance in *p–n* junction under avalanche breakdown condition, part II, *IEEE Trans. Electron Devices,* **ED-13**: 143–151, 1968.
17. R. L. Weirich, Ph.D. Thesis, University College of London, 1971.
18. S. K. Roy et al., Computer methods for the dc field and carrier current profiles in Impatt devices starting from the field extremum in the depletion layer, in *Proc. Int. Conf. Numerical Analysis of Semiconductor Devices (NASECODE I),* Dublin, Ireland, 1979, pp. 266–274.
19. S. P. Pati, J. P. Banerjee, and S. K. Roy, The distribution of negative resistivity in the active layer of millimeter-wave double drift region diode, *J. Phys. D Appl. Phys.,* **22**: 959–964, 1989.
20. H. K. Gummel and J. L. Blue, A small signal theory of avalanche noise in Impatt diodes, *IEEE Trans. Electron Devices,* **ED-14**: 569–580, 1967.
21. S. K. Roy, J. P. Banerjee, and S. P. Pati, A computer analysis of the distribution of high frequency negative resistance in the depletion layer of IMPATT diode, in *Proc. Conf. Numerical Analysis of Semiconductor Devices (NASECODE IV),* Dublin, Ireland, Boole Press, 1985, pp. 494–500.
22. W. J. Evans and G. I. Haddad, A large signal analysis of IMPATT diodes, *IEEE Trans. Electron Devices,* **ED-15**: 708–717, 1968.
23. D. L. Scharfetter and H. K. Gummel, Large signal analysis of a silicon Read diode oscillator, *IEEE Trans. Electron Devices,* **ED-18**: 64–77, 1969.
24. L. C. Chang and D. H. Hu, Large-signal analysis of lo–hi–lo double drift silicon Impatt at 50 GHz, *IEEE Trans. Electron Devices,* **ED-25**: 1137–1140, 1978.
25. P. A. Rolland, C. Dalle, and M. R. Friscourt, Physical understanding and optimum design of high-power millimeter wave pulsed IMPATT diodes, *IEEE Electron Device Lett.,* **12**: 221–223, 1991.
26. T. E. Seidel, R. E. Davis, and D. E. Iglesias, Double drift region ion implanted millimeter wave IMPATT diode, *Proc. IEEE,* **59**: 1222–1228, 1971.
27. K. Nishitani et al., Optimum design for high power and high efficiency GaAs hi–lo IMPATT diodes, *IEEE Trans. Electron Devices,* **ED-26**: 210–214, 1979.
28. M. Sridharan and S. K. Roy, Computer studies on the widening of avalanche zone and decrease of efficiency in silicon X-band sym. DDR, *Electron. Lett.,* **14**: 635–637, 1978.
29. J. P. Banerjee, S. P. Pati, and S. K. Roy, Computer studies on the space charge dependence of avalanche zone width and conversion efficiency of signal drift p^+nn^+ and n^+pp^+ indium phosphide Impatts, *Appl. Phys. A (F.R. Germany),* **35**: 125–128, 1984.
30. M. Sridharan and S. K. Roy, Effect of mobile space charge on the small signal admittance of silicon DDR, *Solid State Electron.,* **23**: 1001–1003, 1980.
31. B. Som, B. B. Pal, and S. K. Roy, A small signal analysis of an IMPATT device having two avalanche layers interspaced by a drift layer, *Solid State Electron.,* **17**: 1029–1058, 1974.
32. N. Mazumdar and S. K. Roy, Studies on pulsed mm wave low–high–low silicon IMPATT diodes at high current density and dependence on structural parameters, *Semiconductor Sci. and Technol.,* **12**: 623–630, 1997.
33. M. E. Elta and G. I. Haddad, High frequency limitations of IMPATT, MITATT and TUNNETT mode devices, *IEEE Trans. Microw. Theory Tech.,* **MTT-27**: 442–449, 1979.

34. M. Mitra et al., Experimental studies on the process steps for fabrication of IMPATT diodes and corresponding study of dc breakdown voltage, *IETE Tech. Rev. (India),* **10** (4): 351–354, 1993.
35. M. S. Gupta, Noise in avalanche transit time devices, *Proc. IEEE,* **59**: 1674–1687, 1971.
36. T. A. Midford and R. L. Bernick, Millimeter wave CW IMPATT diodes and oscillators, *IEEE Trans. Microw. Theory Tech.,* **MTT-27**: 483–491, 1979.
37. T. Misawa and L. P. Marinaccio, 100 GHz Si IMPATT diodes for CW operation, in *Proc. Symp. Submillimeter Waves,* Polytechnic Press of Brooklyn, N.Y., 1970, pp. 53–67.
38. J. F. Luy, W. Behr, and E. Kasper, 90 GHz DDR IMPATT diodes made with Si MBE, *IEEE Trans. Electron Devices,* **ED-34**: 1084–1089, 1987.
39. C. Chao et al., Y-band (170–260 GHz) tunable CW Impatt diode oscillator, *IEEE Trans. Microw. Theory Tech.,* **MTT-25**: 985–991, 1977.
40. T. T. Fong and H. J. Kuno, Millimeter wave pulsed IMPATT source, *IEEE Trans. Microw. Theory Tech.,* **MTT-27**: 492–499, 1979.
41. W. Behr and J. F. Luy, High power operation mode of pulsed IMPATT diodes, *IEEE Electron Device Lett.,* **11**: 206–208, 1990.
42. R. Goldwasser and R. Rosztoczy, High efficiency GaAs lo–hi–lo IMPATT devices by liquid phase epitaxy for X-band, *Appl. Phys. Lett.,* **35**: 92–94, 1974.
43. M. G. Alderstein, R. N. Wallace, and S. R. Steele, Millimeter wave GaAs Read IMPATT diodes, *IEEE Trans. Electron Devices,* **ED-25**: 1151–1156, 1978.
44. P. K. Vasudev, Recent advances in device processing and packaging of high-power pulsed GaAs double drift IMPATTs at X-band, *IEEE. Trans. Electron Devices,* **ED-31**: 1044–1048, 1984.
45. K. Chang et al., GaAs Read-type Impatt diode for 130 GHz CW operation, *Electron. Lett.,* **17**: 471–472, 1981.
46. J. J. Berenz, F. B. Fank, and T. L. Heirl, Ion-implanted p–n junction indium-phosphide IMPATT, *Electron. Lett.,* **14**: 683–684, 1978.
47. J. P. Banerjee, Ph.D. Thesis, Calcutta University, 1984.
48. M. J. Bailey, Heterojunction IMPATT diodes, *IEEE Trans. Electron Devices,* **ED-39**: 1829–1834, 1992.
49. S. K. Roy, B. Som, and B. B. Pal, Dependence of the Read diode characteristics on the current multiplication factor in the avalanche zone, *Proc. IEEE,* **65**: 1072–1075, 1975.
50. N. Mazumder and S. K. Roy, Saturation current induced effects on the microwave and millimeter wave performance of GaAs double drift region IMPATTs, *Int. J. Electron.,* **71**: 227–237, 1991.
51. P. E. Cottrell, J. M. Borrego, and R. J. Gutmann, IMPATT oscillators with enhanced leakage current, *Solid State Electron.,* **18**: 1–12, 1975.
52. H. P. Vyas, Ph.D. Thesis, Rensselaer Polytechnic Institute, Troy, N.Y., 1979.
53. H. P. Vyas, R. J. Gutmann, and J. M. Borrego, Electron and hole photocurrent effects on IMPATT oscillators, *Proc. IEE,* **127**: (Pt. I), 126–132, 1980.
54. N. Mazumder and S. K. Roy, Control of millimeter wave properties of high efficiency double drift region IMPATTs through enhancement of saturation current, *Phys. Stat. Sol. A,* **137**: 267–275, 1993.
55. A. J. Seeds and J. R. Forrest, Initial observations of optical injection locking of an X-band IMPATT oscillator, *Electron. Lett.,* **14**: 829–830, 1978.
56. S. K. Roy, P. K. Goswami, and B. B. Pal, Microwave properties of a proposed Read-like device with variable current multiplication in the avalanche zone and an additional transverse field in the drift-Zone, *Proc. IEEE,* **66**: 92–94, 1978.
57. H. J. Prager, K. K. Chang, and S. Weisbroad, High power high efficiency silicon avalanche diodes at ultra high frequencies, *Proc. IEEE,* **55**: 586–587, 1967.
58. R. L. Johnson, D. L. Scharfetter, and D. J. Bartelink, High efficiency sub transit time oscillations in germanium avalanche diodes, *Proc. IEEE,* **56**: 1611–1613, 1968.
59. D. J. Bartelink and D. L. Scharfetter, Avalanche shock fronts in p–n junctions, *Appl. Phys. Lett.,* **14**: 320–323, 1969.
60. A. S. Chlorofeine, R. J. Ikola, and N. S. Napoli, *RCA Rev.,* **30**: 397–421, 1969.
61. S. G. Liu and J. J. Risko, Fabrication and performance of kilowatt L-band avalanche diodes, *RCA Rev.,* **31**: 3–19, 1970.
62. D. J. Coleman, Jr. and S. M. Sze, A low noise metal semiconductor metal (MSM) microwave oscillator, *Bell Syst. Tech. J.,* **50**: 1675–1695, 1971.
63. S. M. Sze, D. J. Coleman, and A. Loya, Current transport in metal–semiconductor–metal structure, *Solid State Electron.,* **14**: 1209–1218, 1971.
64. J. L. Chu and S. M. Sze, Microwave oscillations in p^+np^+ reachthrough BARITT diode, *Solid State Electron.,* **16**: 85–91, 1973.
65. P. Weissglas, Avalanche and barrier injection devices, in M. J. Howes and D. V. Morgan (eds.), *Microwave Devices,* Wiley, 1976, Chap. 3.
66. S. Ahmad and J. Freyer, High power Pt Schottky BARITT diode, *Electron. Lett.,* **12**: 238–239, 1976.

Reading List

S. Y. Liao, *Microwave Devices and Circuits,* Englewood Cliffs, NJ: Prentice-Hall, 1990.
P. Weissglas, Avalanche and barrier injection devices, in M. J. Howes and D. V. Morgan (eds.), *Microwave Devices,* Wiley, 1976, Chap. 3.
S. M. Sze, *Physics of Semiconductor Devices,* Wiley, 1981.
G. Gibbons, *Avalanche-Diode Microwave Oscillators,* Clarendon Press, Oxford, 1973.

SITESH KUMAR ROY
University of Calcutta

TRANSLATORS. See LOW-POWER BROADCASTING.